
DIPLOMARBEIT

# Assessment of Reed Structure Based on ULS Data

zur Erlangung des akademischen Grades

**Diplom-Ingenieur**

ausgeführt am Department für

Geodäsie und Geoinformation

Forschungsbereich Photogrammetrie

der Technischen Universität Wien

unter Anleitung von

Univ.Prof. Dipl.-Ing. Dr.techn. Norbert Pfeifer

und

Dipl.-Ing. Dr.techn Markus Hollaus

durch

**Vinzenz Schichl**

Matrikelnummer: 01540741

Wien, Dezember 2024 [redacted]

Unterschrift (Verfasser/in) Unterschrift (Betreuer/in)

## Eidesstaatliche Erklärung

Ich erkläre an Eides statt, dass die vorliegende Arbeit nach den anerkannten Grundsätzen für wissenschaftliche Abhandlungen von mir selbstständig erstellt wurde. Alle verwendeten Hilfsmittel, insbesondere die zugrunde gelegte Literatur, sind in dieser Arbeit genannt und aufgelistet. Die aus den Quellen wörtlich entnommenen Stellen, sind als solche kenntlich gemacht.

Das Thema dieser Arbeit wurde von mir bisher weder im In- noch Ausland einer Beurteilerin/einem Beurteiler zur Begutachtung in irgendeiner Form als Prüfungsarbeit vorgelegt. Diese Arbeit stimmt mit der von den Begutachterinnen/Begutachtern beurteilten Arbeit überein.

Wien, im Dezember 2024 

## Acknowledgements

I would like to thank my supervisor, Markus Hollaus, for his constant support throughout this thesis, especially when I faced difficulties and got lost. I also want to thank Gottfried Mandlburger for organizing an additional field campaign in summer, which provided me with the additional data I was looking for.

Graduating at this University would not have been possible without the constant support from my inner circle, motivating me when it was necessary. A special thanks to my brother Florian Etl, who has always supported me with his scientific expertise and endurance when mine was low. Thanks to my parents for their unconditional support throughout my studies, even though I got distracted at times. To Kim for coping with me when nerves got out of hand. Finally to my fellow colleagues and friends Till and Jakob for many shared hours of collective puzzle solving.

## Abstract

The reed belt surrounding Neusiedler See is the largest *Phragmites australis* (Common Reed) reed belt in Central Europe, spanning approximately 180 km². Most of the area is protected as part of the Neusiedler See-Seewinkel National Park. Reduced reed harvesting in recent years, due to warmer winters, has led to the formation of aging and degrading reed stands. Fire management has been proposed as a method to rejuvenate reed stands by eliminating the broken reed layer. To evaluate this method, Land Burgenland conducted a controlled fire experiment on 9 January 2024, accompanied by UAV-based LiDAR and RGB data acquisition before, immediately and several months post-fire. This thesis estimates reed parameters and the structural influence of fire management by computation of topographic models. Further analysis included the vertical point distribution to assess reed parameters, such as the thickness of the broken reed layer and reed density. In-situ data collected by the University of Vienna and BOKU Vienna supported further analysis. A reduction in the thickness of the broken reed layer was quantified using difference DTMs. Validation of the broken reed layer reduction was performed using In-Situ data, collected prior to the fire experiment. In addition, fire-affected areas were successfully quantified, providing further planning data for future fire management campaigns. Reed density assessment was performed using normalized point density values above a height threshold of 100 cm, in an attempt to distinguish dense and sparse reed patches. The absence of In-situ validation data for dense and sparse patches limits the certainty of these classifications. The potential of UAV LiDAR systems for assessing and monitoring reed parameters has been demonstrated.

# Contents

# List of Figures

# List of Tables

# List of Abbreviations

**DSM** Digital Surface Model

**DTM** Digital Terrain Model

**nDSM** normalized Digital Surface Model

**CHM** Canopy Height Model

**ULS** Unmanned Aerial Vehicle Laser Scan

**GPS** Global Positioning Service

**LiDAR** Light Detection and Ranging

**Point Cloud** PC

**Root Mean Square Error** RMSE

# 1 Introduction

The reed belt surrounding Neusiedler See is the largest *Phragmites australis* reed belt in Central Europe, covering approximately 180 square kilometers, with most of the area protected as part of the Neusiedler See-Seewinkel National Park. This region is of great significance for migrating birds, providing essential feeding and breeding sites (Dvorak et al., 2016; Nemeth & Grubbauer, 2005). Its habitat is dominated by *Phragmites australis*-common reed-performing key ecological functions related to water filtration, animal habitat, and shoreline stabilization. However, during the last decades, an overall significant decline in reed harvesting has led to the formation of old and degraded reed stands. This is not only a significant threat to the ecosystem, it also reduces the biodiversity of the affected areas and the habitational quality of the reed belt due to connections between the age structure of the reed and the occurrence of various bird species (Nemeth & Dvorak, 2022).

Modern management methods rule out burning, and other traditional methods, such as reed cutting, have become less effective due to climate change, particularly the lack of ice cover in winter, which is essential for effective reed gathering (Nemeth & Dvorak, 2022). As such, much of the reed belt is facing a transition to a degrading age state, with many stands well over 15 years old and showing signs of reed die-back, the visible retreat or disappearance of mature stands with *P. Australis* within a period of not more than a decade (Dinka et al., 2010; Van Der Putten, 1997). This has been linked to a decline in the bird species typically adapted to old reed stands, further stressing the urgent need for better management methods (Antoniazza et al., 2018).

With the objective of examining the potential benefits of using fire management for the rejuvenation of reed beds, Land Burgenland conducted a controlled fire experiment on 9.1.2024. Such benefits would be the removal of broken reed entirely and therefore reducing the layer between the ground and the stems allowing rejuvenation of old stands.

This experiment was carried out to determine whether a reintroduction of fire management is a method that can be used to rejuvenate old reed stands and effectively remove broken reed. Broken reed, dense reed mats, often formed from old and decaying reed stems, are indicators of habitat deterioration. Their reduction may improve the quality within the reed belt and lead to benefits regarding biodiversity. Researchers suggest that biodiversity in the reed bed is also influenced by other habitat parameters (Nemeth & Dvorak, 2022). These in addition to the broken reed layer consist of open water, standing reed, and bent reed.

The investigation was accompanied by surveys conducted with Unmanned Aerial Vehicles (UAVs) by Skyability GmbH, which utilized LiDAR (ULS) and RGB sensors to collect data both before and after the burn. In August 2024, TU Vienna initiated a third survey campaign, performing another UAV survey in order to obtain more comprehensive data regarding the alterations within the reed bed. In-situ data was collected by University of Vienna and BOKU Vienna. Data collection included ground layer thickness, broken reed layer thickness, as well

as counting the number of reed stalks and measuring reed heights for individual sample plots. The objectives of this thesis are formulated as follows:
- Computation of topographic models within the study area including DSM, DTM and nDSM
- Quantification of burned and unburned areas for evaluation of their effect on the structure of the reed bed with a special focus on the reduction of the broken reed layer
- Identification of other reed characteristics which can be extracted from the available ULS data

The thesis starts with a compact presentation of the current state of the art regarding airborne and UAV data acquisition in combination with LiDAR and RGB sensors, with a special focus on reed habitats. In materials and methods, we focus on a brief overview of the study area, presentation of the sensors used for data collection, and how this data was processed w.r.t. the objectives explained before. In the results section, in addition to the topographic models and the fire area estimate, ULS-derived reed parameters are presented. The discussion focuses on possible improvements regarding in situ data and addresses possible shortcomings in the quantification of reed parameters. Furthermore, the detection of the fire area using topographic models is discussed.

The central question that this research tries to address is:
Can a reduction in the thickness of the broken reed layer caused by fire management be quantified using ULS?

# 2 State of the Art

Using standard consumer grade UAVs in combination with high-quality sensors such as LiDar, GNSS or optical sensors, has introduced many possibilities in scientific fields such as ecological monitoring. This chapter aims to review how UAV applications are currently used in wetland ecosystems with a special focus on areas where common reed (*P. Australis*) can be found.

UAV platforms, equipped with modern and high resolution sensors have appeared, allowing the collection of detailed spatial data within the field of ecological monitoring. This leads to a better understanding of vegetation dynamics and biomass estimation within different fields. Doughty and Cavanaugh (2019) highlight, that UAV imagery can provide high-resolution information on vegetation height and structure, which is very important for biomass estimation in coastal wetlands. Additionally these sensors, mounted on cost-effective platforms can also solve problems present in the use satellite based systems with regard to the spatial resolution and the temporal resolution of large scale remote sensing systems (Gallant, 2015). Furthermore, UAV systems can reduce the amount of time it takes to collect data on the ground and are expected to be critical tools for further monitoring and management of water ecosystems worldwide (Dronova et al., 2021).

Combining LiDAR with UAV systems provides opportunities for different applications. Although it can provide accurate topographic information and information about the structure of vegetation, its penetration is still limited by very dense vegetation. However, in terms of penetrating vegetation and a higher and more uniform point density, LiDAR still offers advantages compared to optical sensors used in photogrammetric approaches (Lin et al., 2019). The most significant advantage lies in its ability to record the vertical structure of vegetation and in it not being limited to the canopy structure, as it is the case when using optical systems (Luo et al., 2017).

Previous studies have used airborne data, but also UAV data in combination with passive (e.g. optical sensors) or active sensors (e.g. LiDAR) to estimate parameters within wetland ecosystems.

ALS-based classification algorithms have previously utilized parameters such as surface reflectance, dropout point count, NDSM height, surface roughness, slope, grid variance, and Sigma Z to classify wetland vegetation. These features were also used to delineate the categories of reed status such as vegetation excluding *P. australis*, healthy *P. australis*, stressed *P. australis*, and stands that suffer from die-back (see Section 1). Maintaining all these classes resulted in an overall classification accuracy of 82.7% with a Cohen's Kappa value of 0.8, indicating good general reliability. Reducing the number of classes improved the classification accuracy to 84%, which is comparable to on-ground methods (Zlinszky et al., 2012). ALS-based LiDAR data was also used to quantify the extent, density, and status of aquatic reed. Point density values and the vertical distribution were used to classify sparse and dense

reed. With an accuracy of 96%, the extent of aquatic reed was determined and could even be sub-classified into sparse and dense patches. However, the precision after subclassification was reduced to 73% compared to measurements on the ground (Corti Meneses et al., 2017). Similar studies focused on deriving the reed status from 3K (camera system) photogrammetric data point clouds computed using Structure from Motion (SfM). In this case a status index was constructed based on reed height, density, extent, and other factors with overall classification accuracy results of the newly proposed reed status index of 81%. In addition, the accuracy of the SfM DSM was evaluated and an overall RMSE of 0.72 m in height was reported in areas dominated by *P. Australis* (Baier et al., 2022).

Another ALS based approach used LiDAR and remotely sensed hyperspectral imagery to estimate the biomass of reed stands. For biomass estimation, LiDAR height and intensity values at different quantiles were combined with vegetation indices computed from hyperspectral data. The results showed an improvement in $R^2$ to 67% when combining these two methods, compared to an $R^2$ of 53/58% (Vegetation Indices only/LiDAR only) (Luo et al., 2017). A combined approach was also used successfully to map the reed bed itself. The best classification results were achieved using compressed spectral data and applying a 'Canopy Height Model' (CHM) from LiDAR data to the classified data. This reduced false classifications when using spectral data only, improving the reed bed classification accuracy from 85% to 97% (Onojeghuo & Blackburn, 2011).

The extent, density and status (vitality) of the reed beds was also determined from RGB UAV data showing comparable results to those presented in Corti Meneses et al., 2018 resulting from a previous ALS campaign. Due to spectral information available in the RGB image based point cloud, vegetation indices were successfully used to quantify vitality, as it is common practice in remote sensing (Huete et al., 2002).

The applications presented previously show that there have been various studies in previous years using passive image-based sensors and LiDAR sensors to assess and classify different parameters important for wetland ecosystems dominated by *P. Australis*. Most studies use airborne data acquisition methods, especially when LiDAR sensors are used. UAV based studies are so far limited to the use of camera systems and lack the employment of UAV mounted LiDAR systems (Corti Meneses et al., 2018; Onojeghuo & Blackburn, 2011; Song et al., 2020). Generally, a higher resolution achieved by the use of UAV-based campaigns could allow for more small-scale analysis, e.g., regarding narrow objects such as reed stems (Baier et al., 2022). So far, high-resolution point clouds have been generated using SfM approaches, showing varying accuracy especially with respect to density estimation (Baier et al., 2022). Ignoring employed sensors, most published works are based on single-date analysis lacking information about potential challenges but also opportunities of UAV based monitoring. Challenges using image sensors include their susceptibility to change in the measurement settings and therefore the need for radiometric calibration between images or normalization between multi-date topographic models. High temporal and spatial resolution

could be named as its most promising opportunities (Dronova et al., 2021).
With a decrease in price for UAV based LiDAR systems, further integration of these systems into already present fine-scale analysis could further improve reed parameter estimation, especially when tested within smaller-scale research areas.

# 3 Materials and Methods

## 3.1 Study Area

The Study area is situated in Seewinkel National Park, close to the town of Jois. The area itself is not directly bordering with the lake but contains water bodies that are connected to each other and the lake itself via streams.
Vegetation is dominated by *P. Australis*, in various different age classes (Nemeth & Dvorak, 2022) and distributions. In a previous study by Csaplovics and Schmidt (2009), 3 reed age classes (III.A, III.Aa and IV.A) were found within the study area. These classes were distinguished using aerial photography and CIR.
Class III.A (310): Poorly developed reed beds with 20-25% emergent plants. Reeds are short and thin, found mainly in the inner reed belt. Only little young reed.
Class III.Aa (311): Subclass of III.A, featuring degraded reed beds in the inner reed belt with a homogeneous structure. Rarely harvested, leading to the predominance of old reeds. Some areas show partial harvesting.
Class IV.A: Sparse reed beds with 30-50% water surface coverage. Dominated by old reeds and subdominant plants. Highly degraded, with areas affected by harvesting.
The age structure of the reed generally shows old age for the study area, with a large part older than 15 years of age back in 2020 (Nemeth & Dvorak, 2022), illustrated in Figure 3.1. Thus, the areas younger than 15 years are now expected to have aged leaving the whole area with reed above 15 years of age.

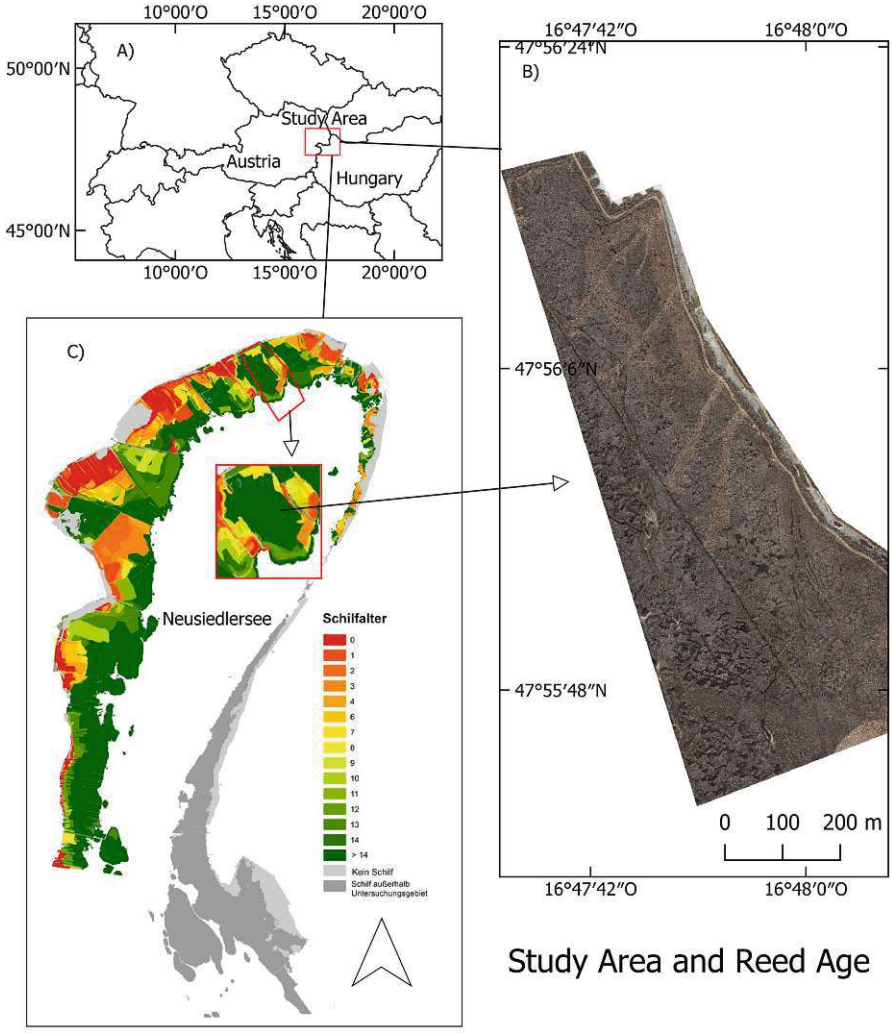


Figure 3.1: A) Overview of the study Area within Europe B) RGB Orthophoto showing the Study Area before the Fire Experiment C) Age structure of the reed belt at Neusiedlersee (Study Area zoomed in View) taken and edited from Nemeth and Dvorak (2022)

## 3.2 Data Collection

The UAV - ULS and RGB mapping was performed by Skyability GmbH as part of the project "Brandschutzübung im Schilfgürtel mit wissenschaftlichem Monitoring". In addition, another UAV - ULS and RGB mapping was performed by staff of TU Vienna. In-Situ data on reed parameters was collected by students of University of Vienna and BOKU Vienna.

### 3.2.1 Sensors and Platform for UAV Data Collection

The ULS Data was collected on 11.1.2024 (ULS1), 26.1.2024 (ULS2) as well as 6.8.2024 (ULS3). ULS1 and ULS2 flights were performed on the same UAV platform, the Skyability

Hammer drone with the RIEGL VUX SYS 1 UAV laserscanner. The specifications of the UAV (Tab. 3.1) as well as the sensor are specified in the tables below (Tab. 3.3).
ULS3 utilized a different Drone and LiDAR scanner, the DJI Enterprise Matrice 350 (see Tab. 3.2) with a Riegl miniVUX-3UAV laserscanner. In order to save data collection time, the RGB image flights were not only performed using the DJI Matrice 350 with a Sony Alpha 6000 but also using a DJI Mavic 3 consumer grade drone with a RTK GNSS sensor and the stock mounted optical sensor.

Table 3.1: Skyability Hammer UAV Specifications

| **Skyability Hammer** | |
|---|---|
| Max. Operating Weight | 25 kg |
| Max. Payload | 16 kg |
| Max. Flight Time | Up to 40 minutes |

Table 3.2: DJI Enterprise Matrice 350 UAV Specifications

| **DJI Matrice Enterprise 350** | |
|---|---|
| Max. Operating Weight | 11 kg |
| Max. Payload | 2.7 kg |
| Max. Flight Time | Up to 55 minutes |

Table 3.3: Parameters of ULS1 & ULS2 LiDAR Flight Setup

| **Parameter** | **Value** |
|---|---|
| Flight Altitude [m] | 120 |
| Flight Speed [m/s] | 8 |
| Scan Angle [degrees] | 80 |
| Scan Frequency [Hz] | 550000 |
| Spot Size ($1/e^2$) [m] | 0.06 |

Table 3.4: Parameters of ULS3 LiDAR Flight Setup

| **Parameter** | **Value** |
|---|---|
| Flight Altitude [m] | 120 |
| Flight Speed [m/s] | 8 |
| Scan Angle [degrees] | 80 |
| Scan Frequency [Hz] | 550000 |
| Spot Size ($1/e^2$) [m] | 0.06 |

The RGB image data was collected once before the fire event, on 11.1.2024 using the DJI M300 UAV platform with a DJI Zenmuse P1 RGB camera. The UAV platform (Tab. 3.5)

and RGB sensor specifications used in the winter data acquisition campaign (Tab. 3.6) on 11.1.2024 are provided below. The parameters for the second RGB flight, in summer on 6.8.2024 are listed below in Tab. 3.7.

Table 3.5: DJI M300 UAV Specifications

| **Parameter** | **Value** |
|---|---|
| Drone Model | DJI M300 |
| Max. Operating Weight | 9 kg |
| Max. Payload | 2.7 kg |
| Max. Flight Time | Up to 45 minutes |

Table 3.6: Parameters of the RGB Flight Setup used on 11.1.2024

| | |
|---|---|
| RGB Flight Altitude [m] | 120 |
| Flight Speed [m/s] | 8 |
| Camera | DJI Zenmuse P1 |
| Lens [mm] | 35 |
| Trigger Interval [s] | 0.7 |
| Ground Footprint [m/Pixel] | 0.015 |

Table 3.7: Parameters of the RGB Flight Setup used on 6.8.2024

| | |
|---|---|
| RGB Flight Altitude [m] | 120 |
| Flight Speed [m/s] | 8 |
| Camera | Sony Alpha A6000 |
| Lens [mm] | 35 |
| Trigger Interval [s] | 0.7 |
| Ground Footprint [m/Pixel] | 0.015 |

### 3.2.2 In-Situ Data

In-Situ data was collected by students and staff from the University of Vienna and BOKU on 10.1.2024 before and on 15.1.2024 after the fire experiment. The data remains unpublished under (Neumann, 2024). Data was gathered at 20 different points across 4 sample areas. The data collection focused on various components of the reed bed: standing reed, broken reed, ground layer, and rhizome.

- **Standing Reed:** This refers to reed stems that are upright and part of the unbroken reed layer. The bent layer is defined as "all non-current-year reed stems inclined at less than 45°, with the reed stems standing crossed in all directions."

- **Broken Reed:** This consists of reeds that are broken flatly in one direction, forming impermeable mats up to 1 meter thick (see Nemeth et al., 2022, p. 28).
- **Ground Layer:** This layer includes decaying organic material that contributes to the soil structure within the reed bed.
- **Rhizome:** The rhizome is the underground part of the reed plant, growing horizontally and producing new shoots.

Regarding our analysis, the focus was on the broken reed layer due to its importance in quantifying the layer before and after burning to evaluate fire management.
For each In-Situ data sample plot within the reed bed, samples were collected to measure both wet and dry masses. In each sample plot, the number of standing reed stems was counted and their heights were measured. Additionally, water depth, soil thickness (ground layer), and the thickness of the broken reed layer were recorded. For this study, only the measured reed heights, water depths, and the thickness of the broken reed and ground layers were analyzed.

## 3.3 Data Processing

Three ULS datasets were provided: ULS1 (before the burning), ULS2 (after the burning) and ULS3 (summer campaign). Data aquisition parameters were previously presented in 3.2.1 (see Tab. 3.3, Tab. 3.6, Tab. 3.1 and Tab. 3.5 for detailed flight parameters of ULS1 and ULS2). Acquisition parameters for ULS3 can be found in Tab. 3.2 and Tab. 3.4.

### 3.3.1 Topographic Data from ULS

#### DSM and nDSM

Using the module opalsDSM, Digital Surface Models (DSM) for all three datasets (ULS1, ULS2 and ULS3) were computed from the ULS point clouds.
OpalsDSM implements the approach suggested by Hollaus et al. (2010), which combines the highest point within a grid cell DSMmax and an interpolated surface DSMmls. The final DSM height is derived based on a surface roughness threshold selecting either DSMmax or DSMmls.
In the case of this study, the parameter 'gridSize' was varied between 0.25 and 2 m in steps of 0.25 m. Hereby, the goal was to capture sufficient detail, yet keeping processing time and noise as low as possible. After testing different parameters, a 1 m 'gridSize' was chosen. It provided enough resolution to identify areas with vegetation, without leaving too many points without data, caused by areas with few echoes, such as water bodies. Figure 3.2 and Figure 3.3 show a 1 m wide profile profile section, of ULS1 and ULS2. After inspection of the point clouds, it becomes clear that a 'gridSize' of 0.25 would potentially create a rather

inhomogeneous surface which as described above is aimed to be avoided for subsequent use of the DSM. We, however, aim to preserve local differences and transitions in reed height by limiting the 'gridSize' to 1 m and not increasing it to 2 m. The 1-meter 'gridSize' was therefore chosen as detailed enough to continue working with it regarding further analysis yet preserving enough level of detail.

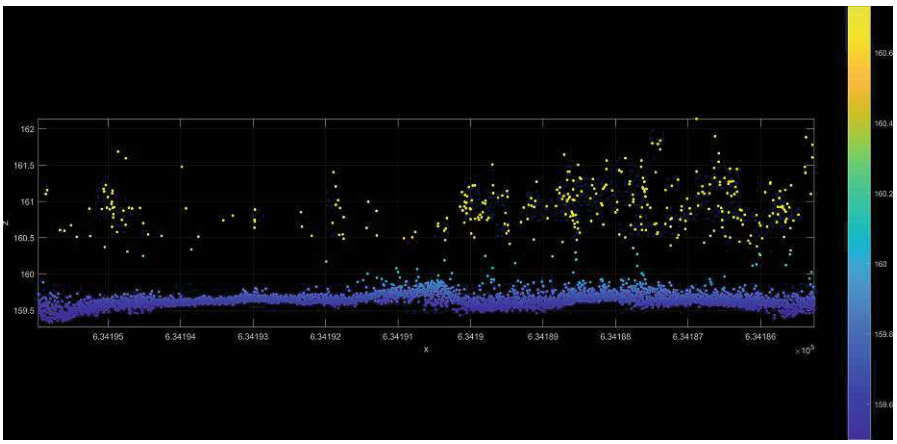


Figure 3.2: 1 m wide Profile of ULS1 showing the Representation of Reed within the Point-cloud (10 m Length)

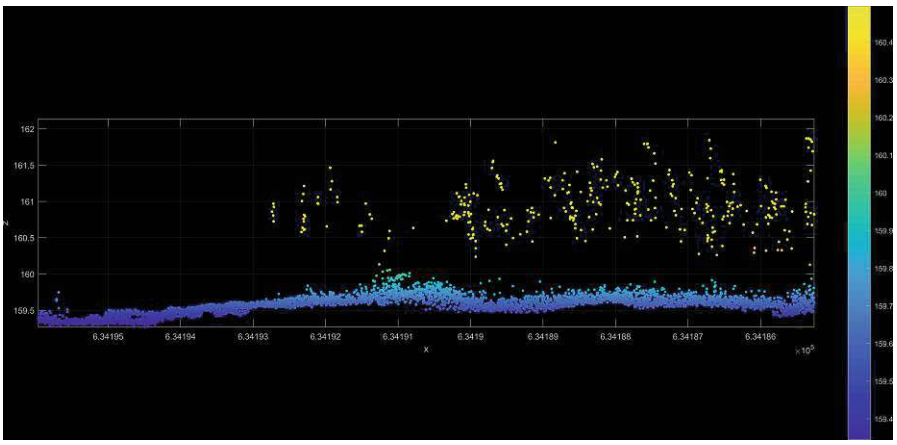


Figure 3.3: 1 m wide Profile of ULS2 showing the Representation of Reed within the Point-cloud (10 m Length)

The number of 'neighbors' was kept at a default value of 8 'neighbors' in order to reduce noise and avoid overfitting.

The DSM heights were normalized using the DTM (as described below in **DTM**), resulting in the computation of an nDSM. For this, the terrain height computed in the DTM was subtracted from the DSM, yielding a normalized surface height.

The accuracy evaluation of the DSM was split into two parts. First, the evaluation of the

height accuracy regarding flat surfaces was computed. For this, the height of the DSM at the checkerboard location was compared with the height measured on site using GNSS measurements.
Second, the height accuracy for areas with reed or vegetation was computed. For this, DSM height measurements were compared with actual In-Situ measurements for reed heights. The mean of the nDSM height within a 1 m diameter was chosen as the normalized height value.
Accuracy measures to be computed, Mean Error and the RMSE as shown in 3.8 were computed for both.
In order to gain information on how the 'gridSize' of the DSM used for the computation of the height values plays a role in the analysis, both a small 'gridSize' 0.25 m nDSM and a 1 m 'gridSize' nDSM were used. For both nDSMs the area of interest (1 m diameter around In-Situ point) and error metrics were computed.

Table 3.8: Error Metrics and Their Formulas (Höhle & Höhle, 2009)

| Metric | Formula |
|---|---|
| Mean Error (Bias) | $\mu = \frac{1}{n}\sum_{i=1}^{n}\Delta h_i$ |
| RMSE | $\text{RMSE} = \sqrt{\frac{1}{n}\sum_{i=1}^{n}(\Delta h_i)^2}$ |

### DTM

For each flight (ULS1, ULS2) an individual DTM was generated using an hierarchical iterative approach implemented in the software OPALS. First, the data was thinned, and the lowest points with a cell size of 0.05 meters (opalsCell) were extracted. After that, the iterative refinement process began with the reduction of data noise and the extraction of ground features using a 3-meter cell size and a 5th quantile feature (opalsCell). A grid was then generated (opalsGrid) and gaps in the grid were filled (opalsFillgaps) using the adaptive fillGaps approach. Normalized Z was computed relative to the initial grid (opalsAddinfo). Iteratively, the grid size, search radii, and neighbor parameters were adjusted in order to refine the DTM. In a last iteration step, the final DTM height was used for normalizing all the points.
Parameters critical in the DTM computation, such as searchRadius and the number of neighbors, were varied in the process. The final parameters were chosen in comparison to the original ULS pointcloud. Different profiles, with varying ground cover (sparse reed, no reed, dense high reed, close to water), were inspected and compared to the ULS pointcloud height and the DTM with the respective parameters. Two profiles were placed on checkerboards used for Orthophoto registration, as shown in Figure 3.4.

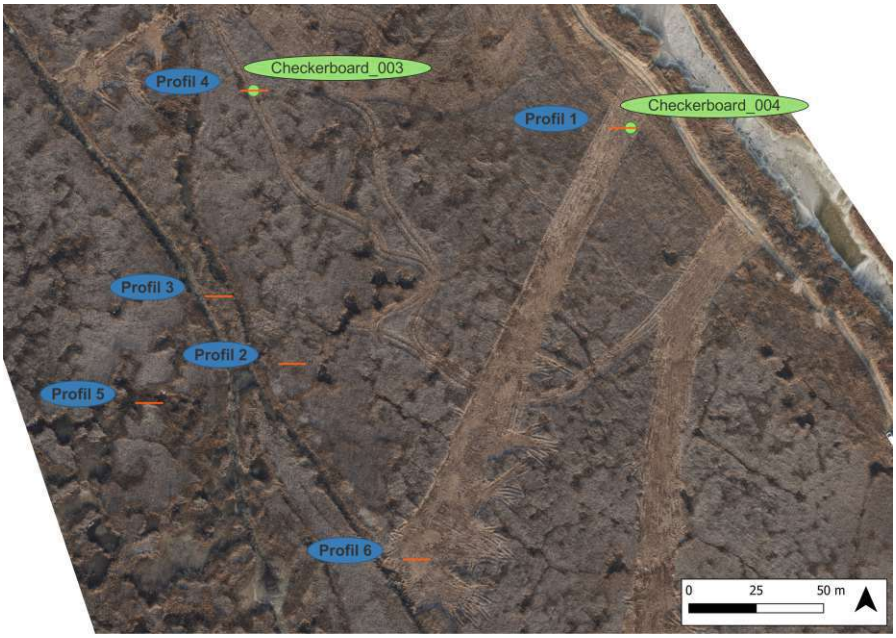


Figure 3.4: Overview of the Profiles inspected throughout the DTM Parameter Testing

Each individual profile has a dimension of 10m*0.25m. While inspecting the different profiles, these were further shortened to 4m and 2m sections to get a better graphical impression of the different DTMs resulting from the tested parameters.
Using a larger search radius and a higher number of neighbors, yielded good results in areas where reed was mowed or very low. However, in areas with high reed the larger search radius lead to excessive values in the DTM (Figure 3.5). This was improved by narrowing the search radius to 0.5 m and decreasing the number of neighbors to 10, as well as increasing the filter from points below 10 cm to points below 5 cm. In areas with high reed, the DTM could be lowered by 5-10 cm with these parameters, whereas in areas without reed a results varied between small increases and decreases (up to 2 cm). The lowering in formerly too low DTM areas proved to be stronger than the negative influence in areas without full grown reed. Therefore, the final parameters were set to a SearchRadius of 0.5m and 10 neighbors.

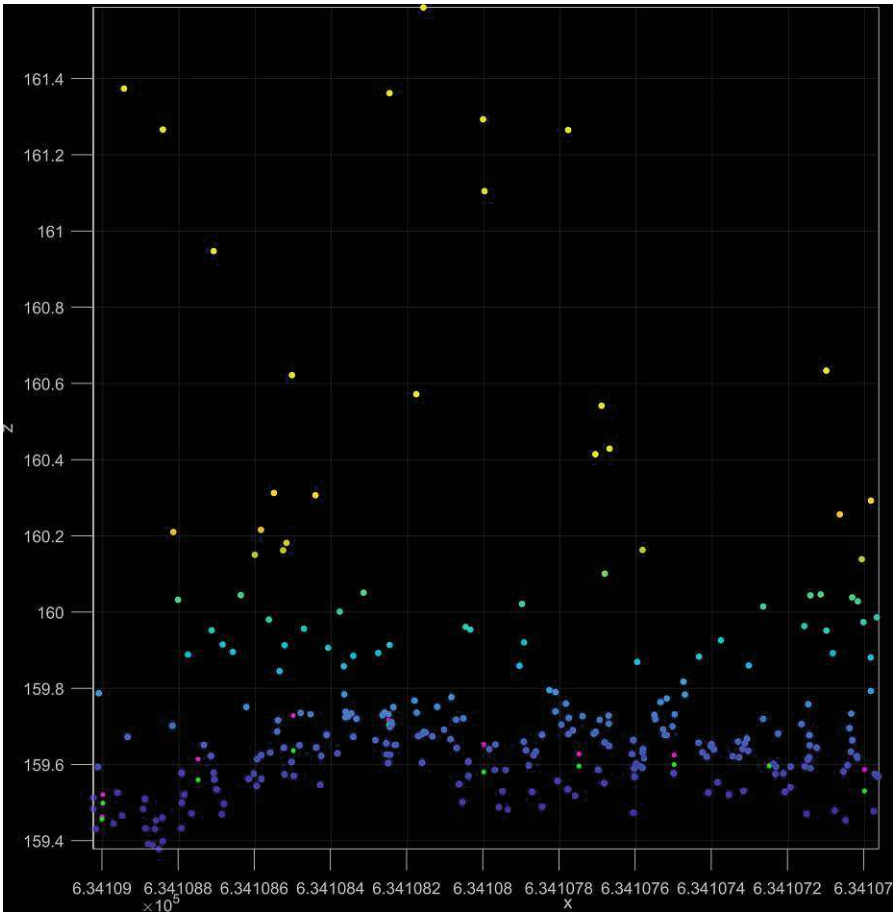


Figure 3.5: Effect of Areas with high Reed on the DTM Height visualized in Profile 3 and a Length of 2 m. (Magenta/Green: SR1/SR0.5 and 30/10 Neighbors)

### 3.3.2 Fire Area Estimation

The estimation of areas that have been burned during the controlled burning attempt was also subject to the data analysis. Hereby not only the total burned area was of interest, but also areas within the burned areas that did not fully burn. Such, "No Burn Areas" as well as water bodies were taken into account in the following step to calculate the burned biomass. Burned areas were computed by analyzing the difference between the DSM before and after the burning. After the computation of the difference DSM, a threshold was chosen to identify areas where burning occurred. This value was set to 80 cm, meaning areas with a change of >= 80 cm were classified as burned areas. This threshold, in comparison with the difference DSM showed good agreement as seen in Figure 3.6. Areas without change are not detected as burned areas.

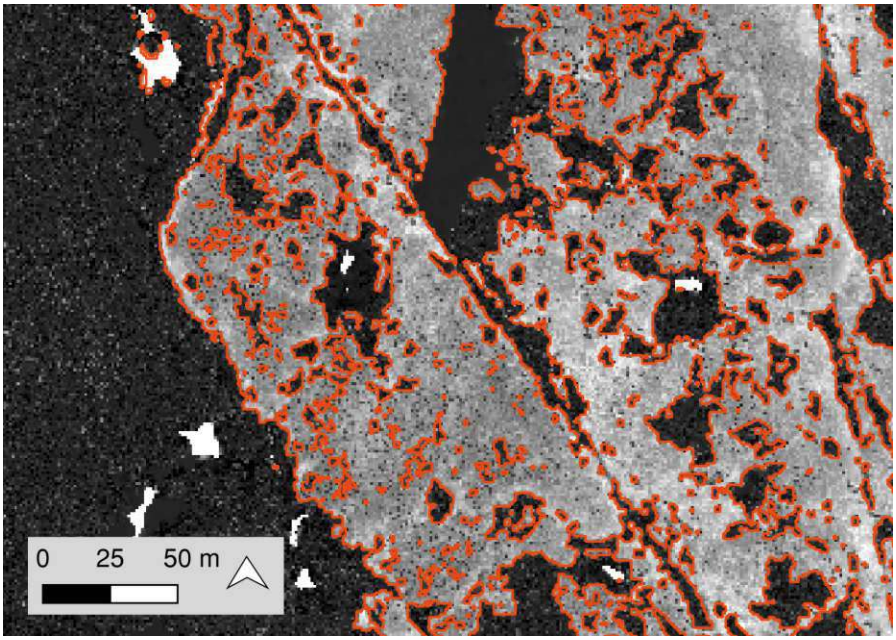


Figure 3.6: Comparison of Burned Areas (red polygons) with Difference of the DSM computed from ULS1 and ULS2

Using the software 'CloudCompare', the classified areas were further cleaned, eliminating large areas that were not part of the measuring site, as well as single pixels that were classified as burned. In order to be able to compare the total burned areas, the outer contour of three large individual burned areas was computed (Figure 3.7) and compared with the classification area taking into account areas not fully burned. In addition, water areas were subtracted from the outer contour polygons used for the area computation.

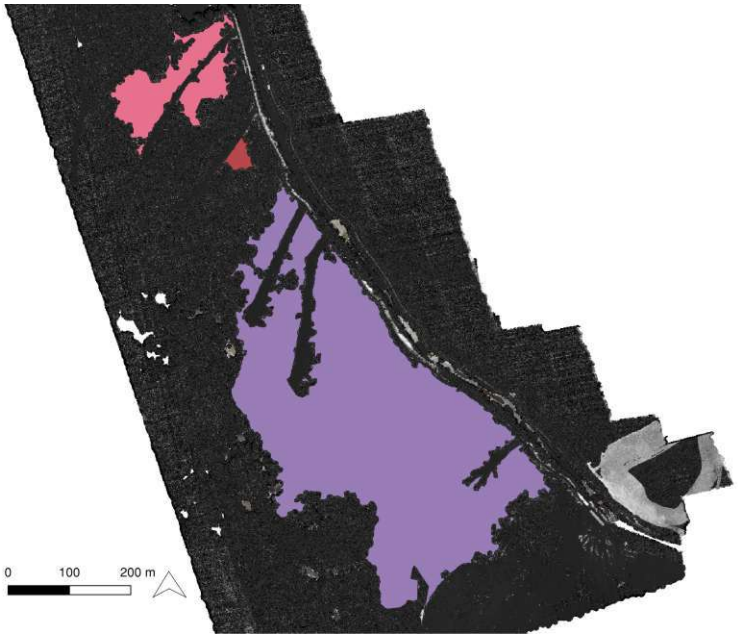


Figure 3.7: Polygons used for Calculation of Total Area that has been affected by Burning throughout the Fire

### 3.3.3 Co-Registration of In-Situ Data and ULS Data

GPS coordinates were captured using a handheld GPS device, which provided an estimated positioning accuracy of up to 4 meters (Schaefer & Pearson, 2021), compared to the ULS and RGB accuracy of <5 cm. In-Situ Data Points were visualized using circles with a radius of 7.5m. As the in situ coordinates and the ULS data have different positioning precisions, a radius of 7.5 m was used to account for the positioning uncertainty of the GPS device, ensuring that the In-Situ data sample plot falls within the circle. If possible, the exact location of the In-Situ sample plot was determined using visual inspection of the RGB orthophoto collected on 11.1.2024.

Figure 3.8 illustrates the workflow to identify the exact locations where In-Situ data was collected. First, a rough estimate of a circle with a radius of 7.5 m around the GPS location was used. In two additional steps, we searched for square-shaped holes made by a spade and compared them with the data acquisition photos.


Figure 3.8: Workflow Finding the Exact Locations of In-Situ Data Points through Visual Inspection of the In-Situ Areas Step 1: Identification of potential Area through footpaths and holes Step 2: Further Analysis of Holes searching for Square Structures from Spade Step 3: Adding Point Location in the center of Identified Hole

In order to get a first overview on the effects of the fire, the difference in the DTM heights between ULS1 and ULS2 was computed within both a 7.5 m radius and where possible, due to finding the exact point location, a 1 m radius. Statistical values (median, mean) were computed to capture the range of values. In total, 4 In-Situ data collection locations were identified within the areas previously classified as affected by fire. In situ points 12, 15, 17, 20 (green) were used for further analysis of the changes in broken reed illustrated in the map in Figure 3.9.

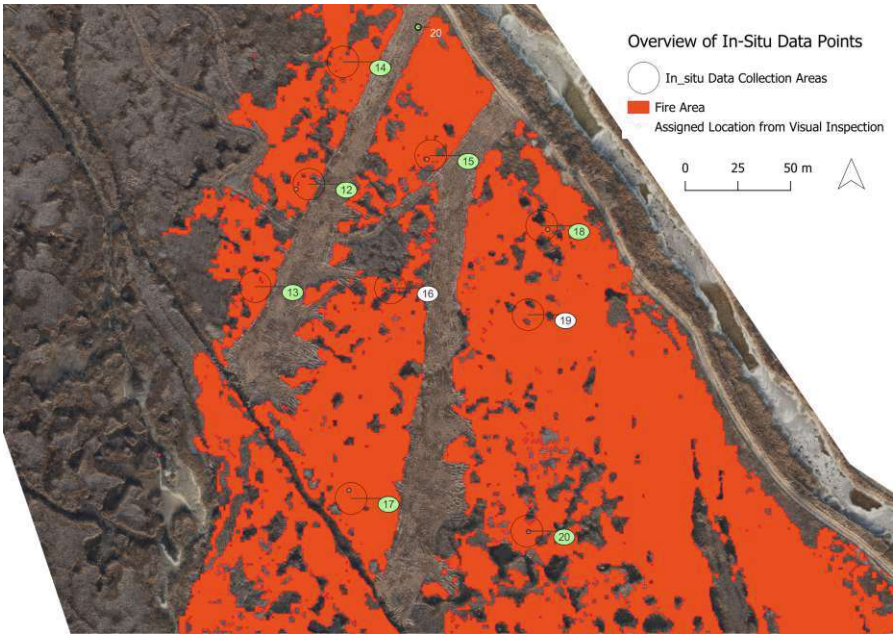


Figure 3.9: Overview of the Areas affected by Fire and In-Situ Data Points (green Points used for further Analysis)

### 3.3.4 Detection of Water Bodies

In order to be able to further compare areas where burning was classified, water bodies were also delineated. This was done using the DSM as well as threshold values for the water level (Hydrographischer Dienst Burgenland, 2024b).These water level observations were furthermore compared to precipitation data (Hydrographischer Dienst Burgenland, 2024a) during the two UAV flights.

Two different stations were used as references for the measurements: water level data was obtained from Station Breitenbrunn, and precipitation data was obtained from Station Neusiedl am See. Between the first flight date (ULS1) and the second flight date (ULS2), the water level showed a rise of 20 mm, accompanied by a total precipitation of 15.4 mm (Figure 3.10). The average monthly rainfall for this period of time is 14.6 mm.

According to Hackl and Ledolter (2023), a rise in water level of 5 mm per 10 mm of average monthly precipitation is proposed. Given this relationship, the observed increase in water level between the two flight dates is higher than what we would expect from precipitation data. After investigating Figure 3.10, we can see that precipitation does not immediately affect the water level observed at the station.

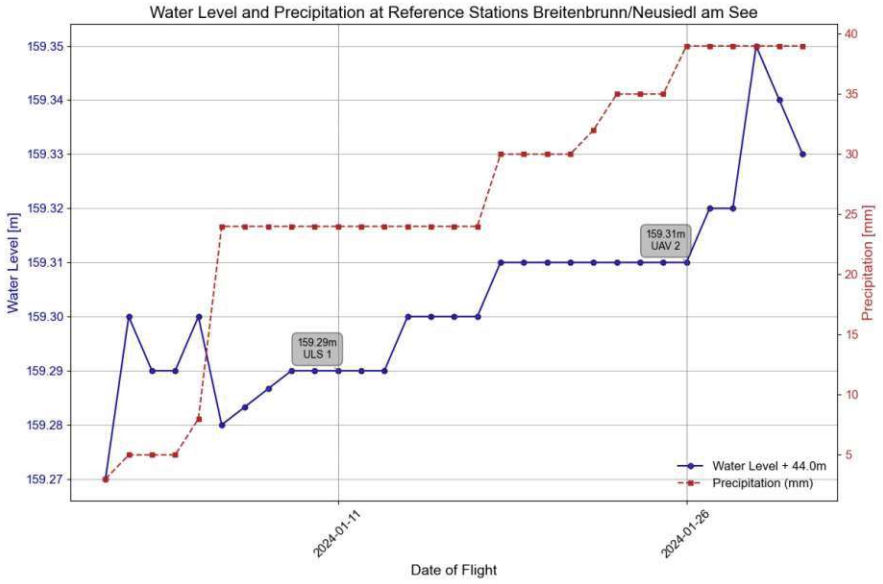


Figure 3.10: Water Level and Precipitation at Station Breitenbrunn and Neusiedl am See, Data courtesy of Hydrographischer Dienst Burgenland (2024b).

The height values at Breitenbrunn station were adjusted to align with EVRS heights derived from the point cloud data using the official height transformation grid (BEV - Bundesamt für Eich- und Vermessungswesen, 2024). A correction of 44.00 m was applied to convert the heights from the local datum (müA) to the Amsterdam Ordnance Datum (NAP) of the DTM. To estimate the extent of water bodies within the measurement area, we used the DTM, which should only represent ground points. This approach should make it easier to identify narrow water bodies, overshadowed with reed areas. Consequently, water- land borders are expected to be represented more clearly.

The threshold value for classifying points as water was determined by comparing the heights in the DTM corresponding to known water bodies and referencing them against observed water levels, as shown in Figure 3.10.

ULS2 DTM was used for the computation of the water areas, because due to burning, the overgrowth around the small streams was reduced and therefore the water-land border is represented more clearly. However, it is important to note that DTM heights do not necessarily correspond exactly to water surface levels due to various factors such as local differences between the water level of Lake Neusiedl and the ponds and streams that pass through the measurement site. Therefore, a threshold of an estimated water height of 159.30 m+0.1 m and -0.3 m was applied.

To include potential variations and ensure a more realistic water detection, all points in the DTM lower than 159.3 m by 30 cm or more were classified as water.

With this approach, our objective was to combine the real terrain data of the DTM with nearby water level observations to delineate water bodies within the study area.

### 3.3.5 Detection of Different Reed Habitat Variables

As described in Section 3.2.2, the reed bed consists of various components (habitat variables), such as standing reed and broken reed (Nemeth et al., 2022).

#### Estimation of Broken Reed Layer Thickness

The quantification of the broken reed layer (as defined in Section 3.2.2) was conducted using the raw point clouds from each ULS flight. For each In-Situ data point, the thickness of the broken reed layer was measured.

This measurement involved comparing In-Situ data points collected before and after the fire event. The depth recorded before the fire not only reflects the thickness of the broken reed layer but also includes the underlying ground layer. To isolate the broken reed layer, we compared the combined thickness of the broken reed and ground layers before the fire with the corresponding thickness after the fire. This comparison allowed us to determine the thickness of the broken reed layer by subtracting the post-fire measurements, specifically accounting for changes attributed to the fire event.

The hole depth was computed using height values of two quantiles to achieve a reproducible and unbiased assessment, avoiding reliance on individual data points. For each In-Situ data point, the starting point of the broken reed layer and the lowest points within the hole were recorded. To accurately identify the bottom points, the 1% quantile was used. Thus, minimizing the influence of outliers while keeping enough data points, especially given the low number of points at the bottom of each hole.

Determining the top of the hole was more challenging, as it required selecting a percentile that would minimize the impact of reed stems and the area surrounding the hole, while providing realistic approximations. 3 different percentiles were tested (90%, 80%, 70%), as shown in Figure 3.11. After further inspection, the 70% percentile was chosen for the top measurement, as it offered the best balance by reducing the influence from reed stems and only selecting points within the hole, leading to a more realistic top value estimate.

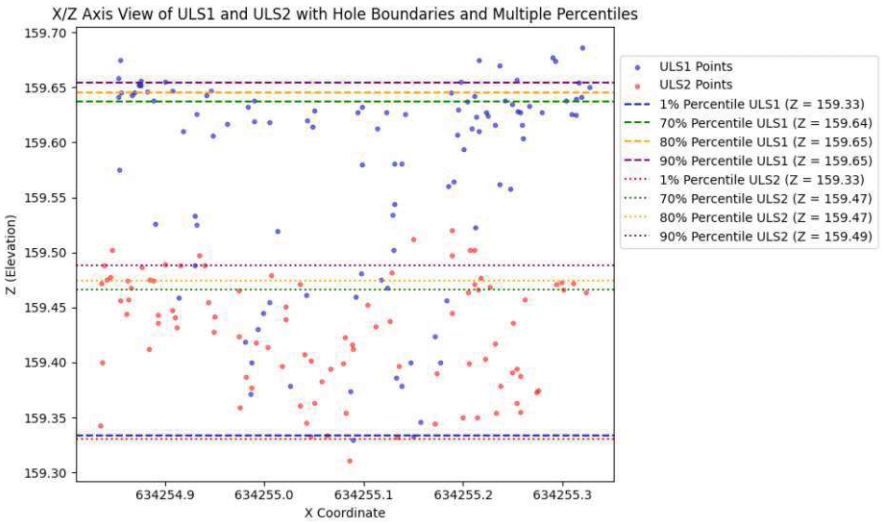


Figure 3.11: Plot of In-Situ PNR17 from ULS1 and ULS2 and the 90%, 80%, 70% and 1% Percentiles used for the determination of the Hole Bottom and Top

The limits calculated before are subsequently used to derive the thickness of the broken reed layer as well as the ground layer directly from the point cloud.

The parameters for estimating the broken reed and ground layer are computed as follows.

**1. Broken Reed Layer Thickness:** The thickness of the broken reed layer was calculated as the difference between the 70% percentile values of ULS1 and ULS2, represented by Equation 3.1:

$$\text{Broken Reed Layer Thickness} = \text{Percentile}_{70\%}(\text{ULS1}) - \text{Percentile}_{70\%}(\text{ULS2}) \quad (3.1)$$

**2. Total Thickness (Before Fire):** The overall thickness before the fire was determined by calculating the difference between the 70% percentile of ULS1 and the minimum of the 1st percentiles of ULS1 and ULS2, as shown in Equation 3.2:

$$\text{Total Thickness} = \text{Percentile}_{70\%}(\text{ULS1}) - \min\left(\text{Percentile}_{1\%}(\text{ULS1}), \text{Percentile}_{1\%}(\text{ULS2})\right) \quad (3.2)$$

**3. Ground Layer Thickness:** The thickness of the ground layer was obtained by subtracting the broken reed layer thickness from the overall thickness, as indicated in Equation 3.3:

$$\text{Ground Layer Thickness} = \text{Overall Thickness} - \text{Broken Reed Layer Thickness} \quad (3.3)$$

### Reed Density

Aging reed and the previously discussed reed habitat parameters significantly influence the way different species populate the reed belt. As noted previously, the density of reed stands is a factor in characterizing the reed stands (sparse / dense) (Grosser et al., 1997).
The number of reed stalks and therefore the amount of standing reed is an important habitat variable and was collected as In-Situ data. Classification of large areas w.r.t the number of reed stalks due to the geometry of a reed stalk will not be possible on the level of individual stalks. An attempt was therefore made to find a similar solution as suggested by Corti Meneses et al., 2017, where reed was classified into dense and sparse patches.

#### Process of Normalizing the Point Density

To ensure that point density values were comparable throughout the study area, a normalization process was performed. Without normalization, point density can be affected by variations in UAV flight parameters, vegetation density, or differences in flight paths.
After visualizing the first return point density using a 1 m grid cell size, distinct flight patterns can be observed. These flight patterns, as previously explained, make the point density values from different locations inconsistent and incomparable.

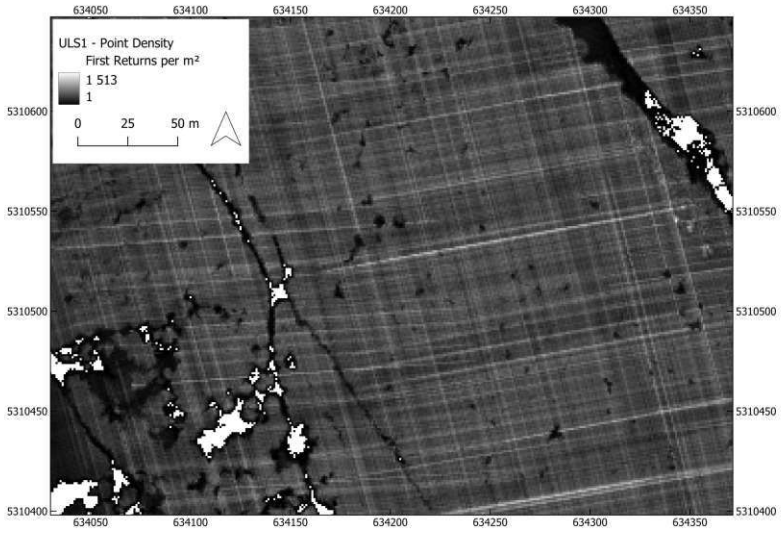


Figure 3.12: Point Density of First returns only without further constraints. Clearly flight patterns can be observed.

Figure 3.12 illustrates these flight patterns. To reduce their impact and make the point density more comparable, additional normalization steps were necessary.
Subsequently, a first return point density map was created, this time including only points

that were at least 10 cm above the ground (using the nDSM calculated beforehand, see Section 3.3.1 for details). Again, a 1 m grid size was used. The height value was set as to exclude points on the ground. Furthermore, the same procedure was repeated for heights >50/100/150 cm, in order to get an overview of how points are distributed above certain thresholds. These absolute point density numbers above certain thresholds are then divided by the total number of first returns for the respective grid cell. This results in a relative point density map for each threshold, which shows the percentage of the number of points above a certain threshold, to the total number of first returns. High percentages indicate an accumulation above the respective threshold, and low values indicate an accumulation of points on the ground. Figure 3.13 shows four different point density maps, it can be clearly observed that thresholds above 50 cm lead to large gaps in the analysis.

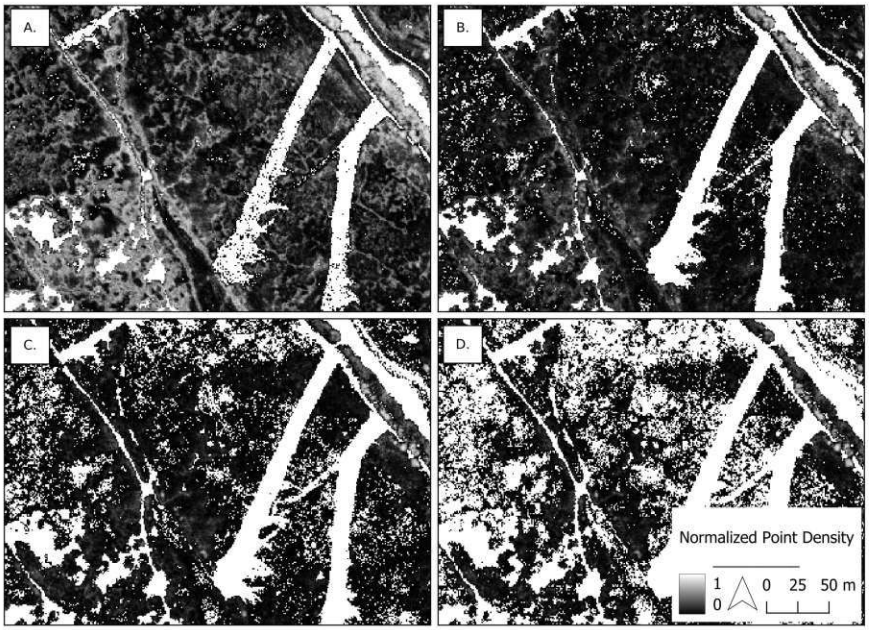


Figure 3.13: Comparison of relative point density maps at different height thresholds. A. shows the point density excluding all points below 0.1 m, B. excludes points below 0.5 m, C. excludes points below 1 m, and D. excludes points below 1.5 m. This visualization highlights how varying height thresholds influence the resulting point density distributions.

As shown in Figure 3.14, the normalized point density values above the normalized terrain height of 10 cm show significantly fewer indications of flight path influence.
The point density in dense reed stocks tends to accumulate in a height > 1.5 m due to the

large number of leaves above this height and bare stems below (Corti Meneses et al., 2017). In sparse stocks, the point distribution is equal and there is no such accumulation. This is because of bigger structures in the higher part of the reed canopy such as flowers, seeds, or leaves, which are as frequent in winter.
Increasing the height of the border to upwards of 0.5 m leads to low point density values due to missing large structures such as leaves in the upper part of the reed.

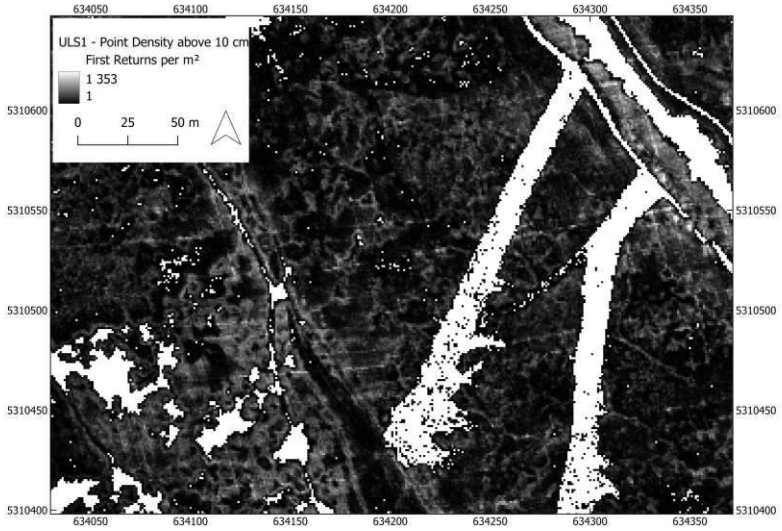


Figure 3.14: Point Density of First returns higher than 10 cm w.r.t. to the nDSM computed beforehand

Using Figures 3.12 and 3.14, a relative point density map was generated above the respective height threshold, as shown in Figure 3.15. These relative point density maps serve as a basis for further analyses.

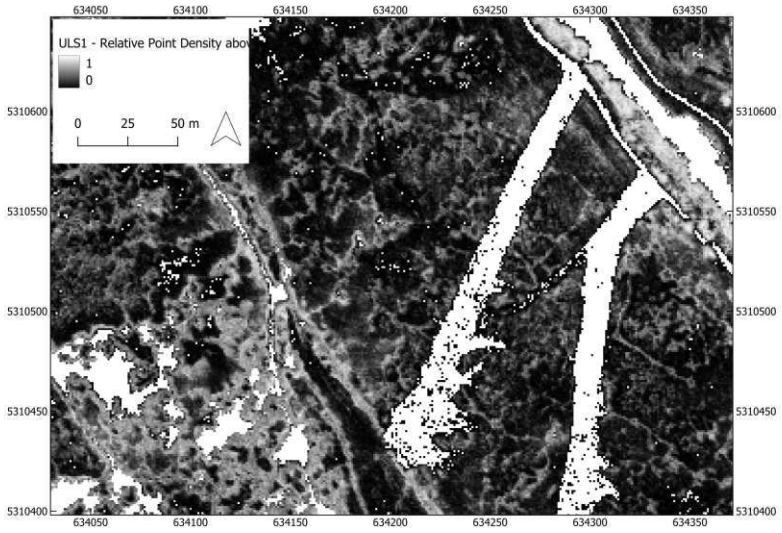


Figure 3.15: Relative Point Density Map for further Analyses

**Thresholds For Classification**

Due to differences regarding the flight parameters as well as seasonal variations regarding the data collection time (ULS1 and ULS2) it was not possible to use thresholds previously used in Corti Meneses et al., 2017. The mentioned study suggests an approach using absolute point density values combined with rank statistics within a local neighborhood. In our approach as stated before, point density values are normalized and rasterized in 1x1 m raster cells.

The challenge therefore lies in finding suitable relative point density thresholds that can be used to describe the distribution of standing reed throughout the study area. Specifically on how the reed was distributed before the fire event.

Table 3.9 compares the relative point density computed from the ULS1 pointcloud with actual In-Situ measurements. The stalks were counted in 25x25 cm areas and then multiplied in order to get the number per $m^2$. The values show that there is no correlation between the number of In-Situ measured stalks and the point density. A threshold w.r.t to the number of stalks therefore is not meaningful.

| In-Situ PNR | Normalized Point Density above 10 cm | Stalks/m² |
|---|---|---|
| 12 | 0.09 | 48 |
| 15 | 0.09 | 256 |
| 6 | 0.07 | 112 |
| 5 | 0.06 | 48 |
| 18 | 0.06 | 112 |
| 4 | 0.03 | 192 |
| 17 | 0.01 | 192 |
| 20 | 0.01 | 112 |

Table 3.9: Pre-Fire reed stalks/m² compared with relative In-Situ Values computed from the ULS1 Pointcloud

As described above, the number of points in the upper part of the canopy is rather small for ULS1 and ULS2. Therefore, no suitable threshold for the classification w.r.t. point density can be found. Figure 3.16 clearly shows how during the winter months the points accumulate on the ground, whereas in summer there are hardly any points on the ground. However, we can clearly see a change in the vertical distribution of the points depending on vegetation height. Dense stocks tend to accumulate points above a height of 1.5 meters and hardly have any points on the stems. Sparse stocks have a uniform distribution with a lower overall height (Corti Meneses et al., 2017).

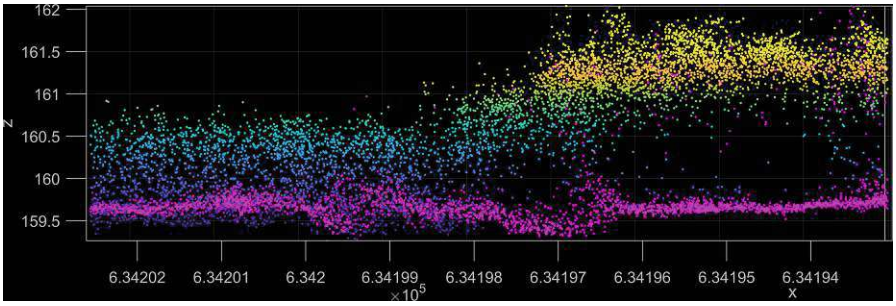


Figure 3.16: Pointclouds of ULS1 (magenta) and ULS3 (Z-colorcoded) compared

Figure 3.17 shows the normalized point density for ULS3 above 1.5 m and additionally the areas previously affected by fire.
When computing the normalized point density above 1.5 m for ULS3 we can notice patches with low relative point density, some with higher point density and some large data gaps. The data gaps occur due to a low amount of points above this height.

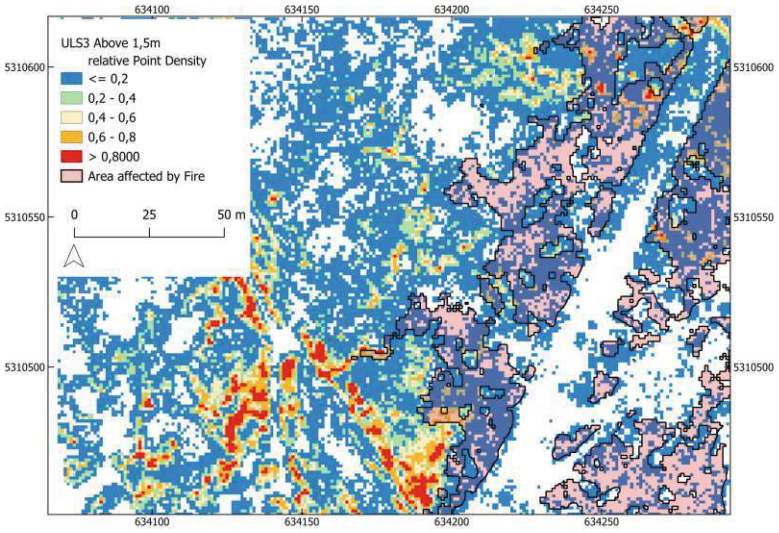


Figure 3.17: Normalized Point Density for a height over 1.5 m

The height threshold was reduced to 1 m, aiming to get a better coverage throughout the study area. Additionally the classes, as well as their limits have been altered to reflect how the vertical point distribution is expected (as explained above).

| Relative Point Density Thresholds for Sparse and Dense Reed | Description |
|---|---|
| <0.05 | No Reed |
| 0.05 - 0.5 | Sparse Reed |
| >0.5 | Dense Reed |

Table 3.10: Classification of Relative Point Density above 1 m

# 4 Results

## 4.1 DSM

As mentioned previously, for each ULS flight, a DSM was calculated. For DSM computation, as mentioned in Section 3.3.1, different GridSizes were used within the OpalsDSM module. The results have shown that in order to limit gaps and make the DSM more homogeneous, larger GridSizes are favored.

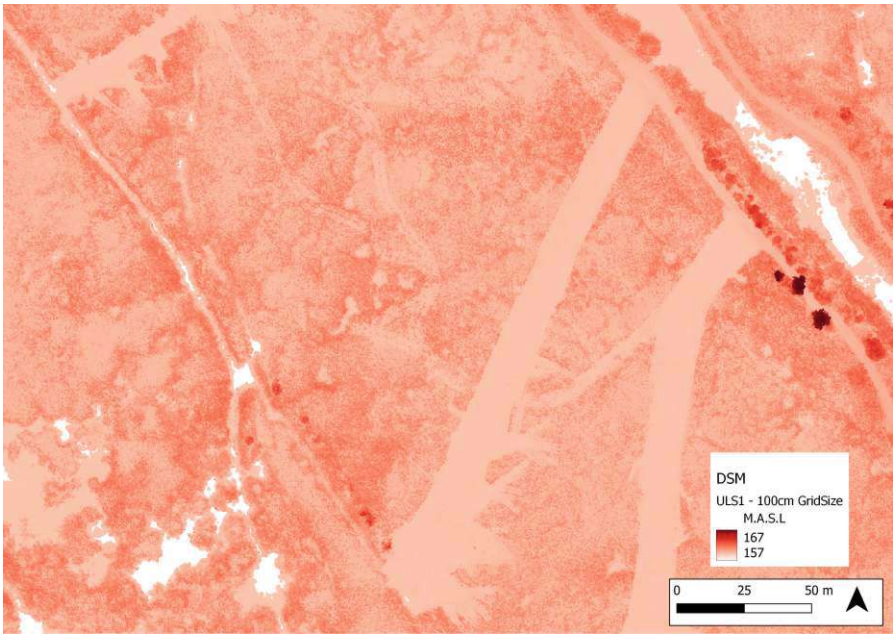


Figure 4.1: DSM of Parts of ULS1 Computed using a GridSize of 25cm in OpalsDSM Module

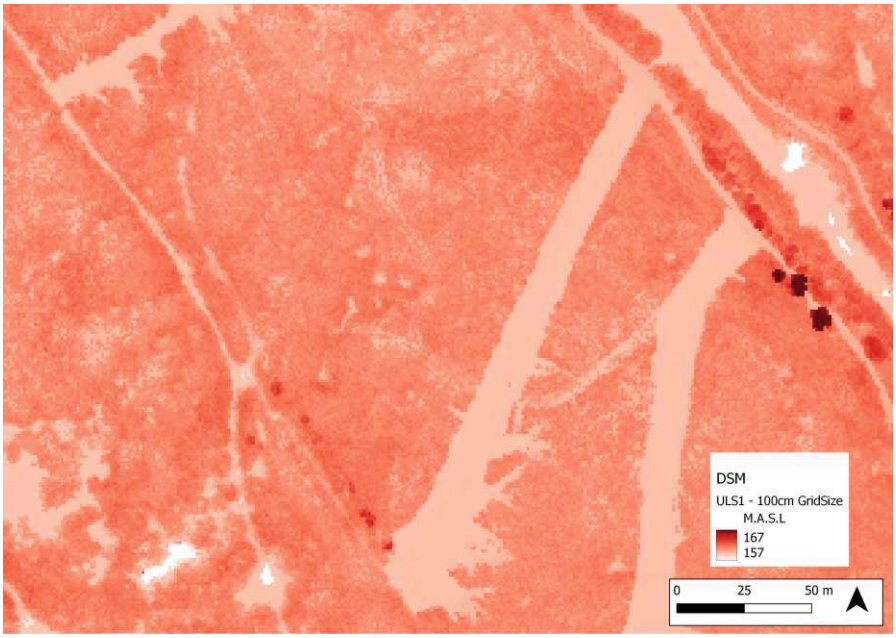


Figure 4.2: DSM of Parts of ULS1 Computed using a GridSize of 100cm in OpalsDSM Module

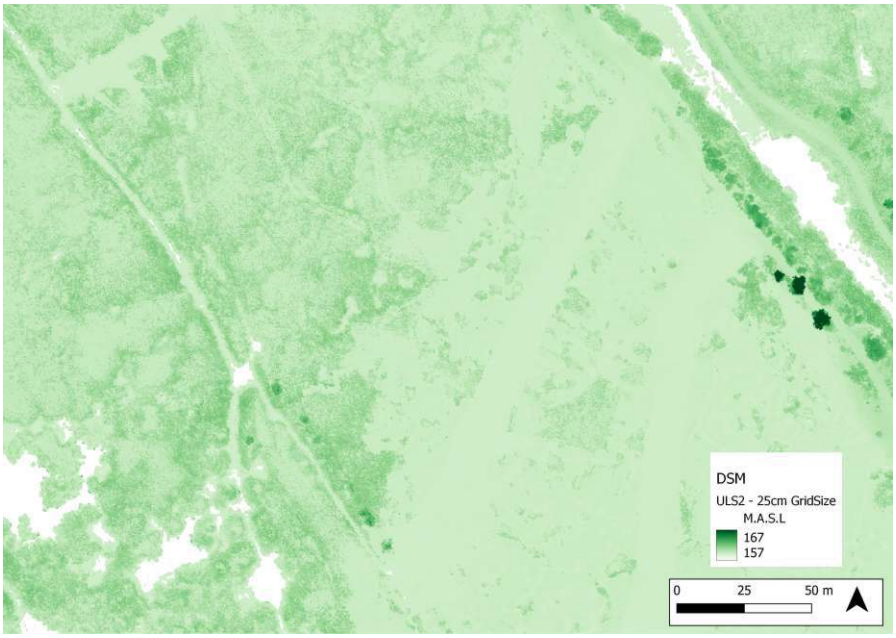


Figure 4.3: DSM of Parts of ULS2 Computed using a GridSize of 25cm in OpalsDSM Module

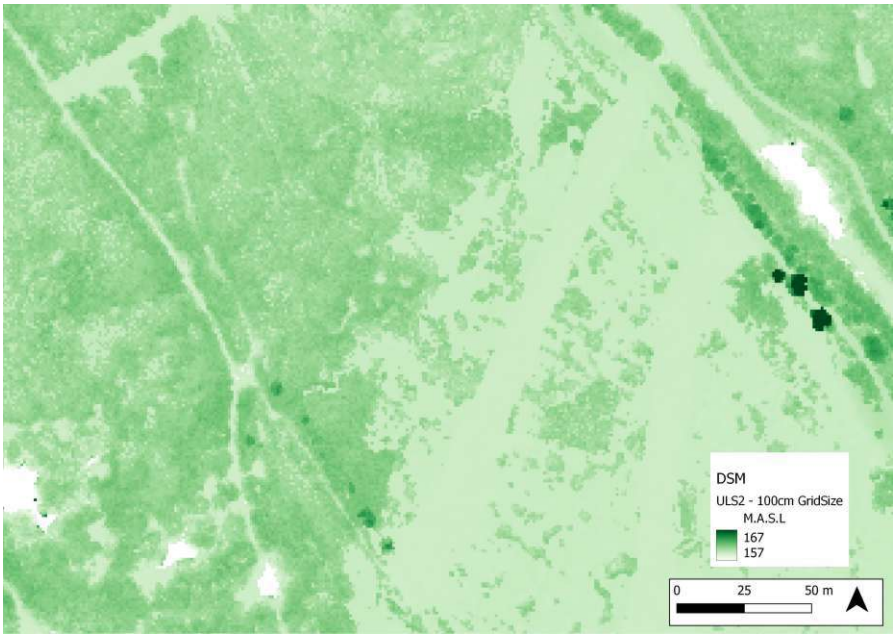


Figure 4.4: DSM of Parts of ULS2 Computed using a GridSize of 100cm in OpalsDSM Module

Comparing Figure 4.1 and Figure 4.2 one can clearly see that with a bigger grid size, details are lost, but the DSM itself becomes more homogeneous. This homogeneity has advantages when computing the difference DSM used for the segmentation of the data into burned and unburned areas.

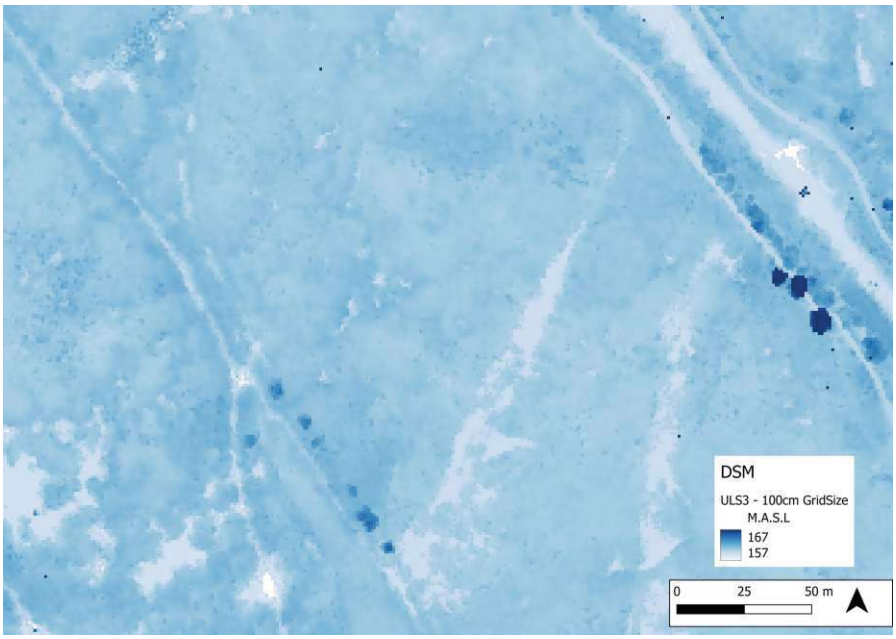


Figure 4.5: DSM of Parts of ULS3 Computed using a GridSize of 25 cm in OpalsDSM Module

Figure 4.5 shows the DSM computed from the scan of August 2024. It shows that during summer months, the vegetative season, the reed has regrown in areas where burning was detected. Furthermore, the borders between areas that burned and those that did not get affected by burning become difficult to observe.

### 4.1.1 Accuracy Assessment of DSM

The accuracy of the DSM was evaluated in two parts. Part 1 was the evaluation of the accuracy regarding flat surfaces. For this, the height of the DSM on checkerboards was compared with the height measured on site using GNSS measurements.
Part 2 was the evaluation of the accuracy of the DSM height in reed covered areas, compared with those obtained from In-Situ measurements.
Tab. 4.1 shows the results in Terms vertical DSM accuracy of RMSE and bias using a 0.25 m gridSize DSM. It clearly shows that the values of the reed height as measured In-Situ, do not match the heights computed in the DSM. Flat areas such as the checkerboards show good alignment. Increasing the gridSize significantly reduces the RMSE and also the bias.

Table 4.1: Vertical Accuracy Asessment for 0.25m nDSM/DSM Gridsize

| **Source** | **Bias [m]** | **RMSE [m]** |
|---|---|---|
| Flat Areas | 0.01 | 0.01 |
| Areas with Grown Reed | -0.98 | 0.99 |

Table 4.2: Vertical Accuracy Asessment for 1m nDSM Gridsize

| **Source** | **Bias [m]** | **RMSE [m]** |
|---|---|---|
| Flat Areas | -0.12 | 0.24 |
| Areas with Grown Reed | -0.11 | 0.42 |

The results on flat surfaces revealed good vertical alignment with the GNSS measurements.

## 4.2 DTM

For each of the two ULS flights in winter, a DTM was computed. The final DTMs for each flight are shown below in Figure 4.6 and Figure 4.7. Small differences in the DTMs were expected, however large differences of around 10-50 cm are visible in areas where reed was burned, indicating a significant reduction of terrain height, caused by the fire event.

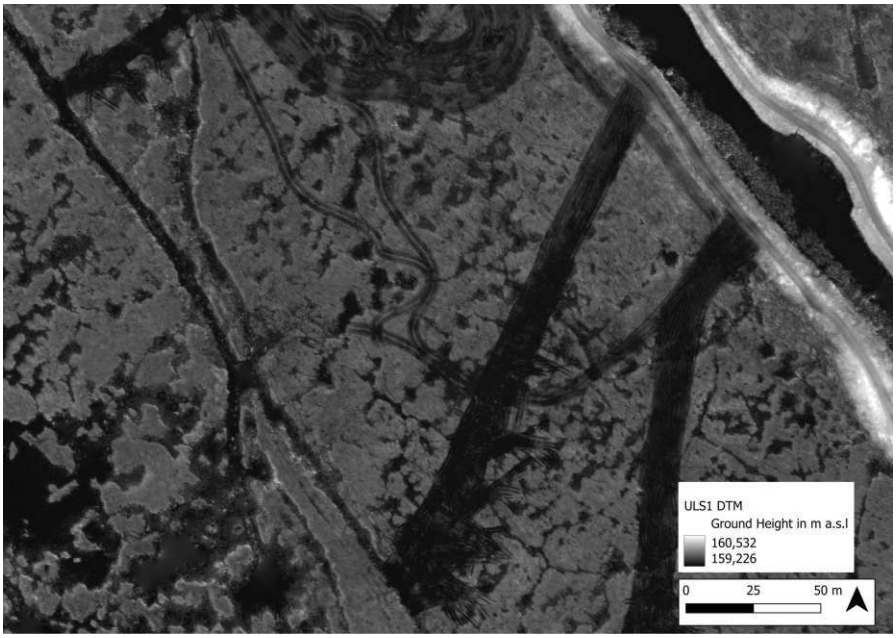


Figure 4.6: DTM of Parts of ULS1

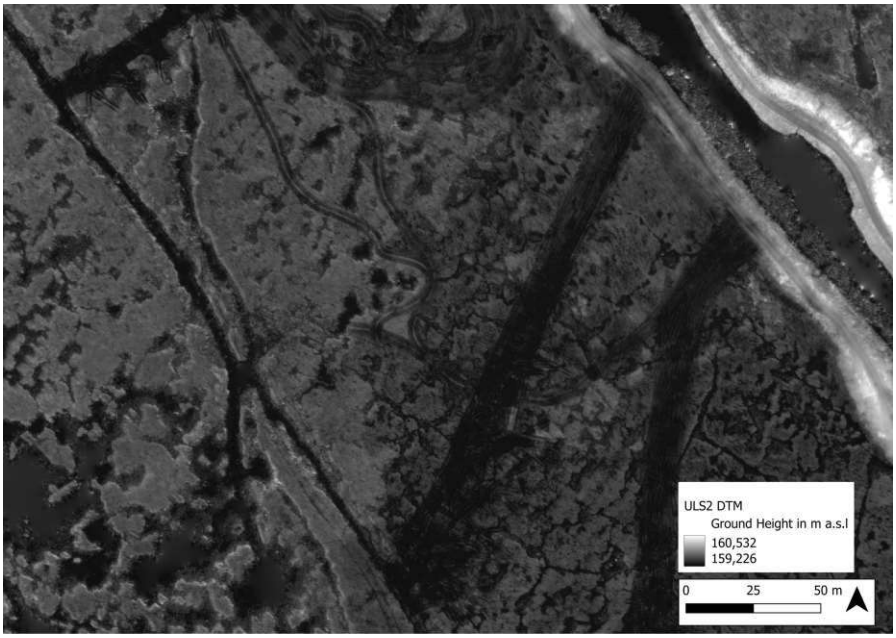


Figure 4.7: DTM of Parts of ULS2

This reduction in terrain height becomes even more visible when computing a difference DTM, where positive values indicate a reduced terrain height. Figure 4.8 shows the difference DTM computed for parts of the study area clearly, indicating areas where height reduction in the DTM took place.

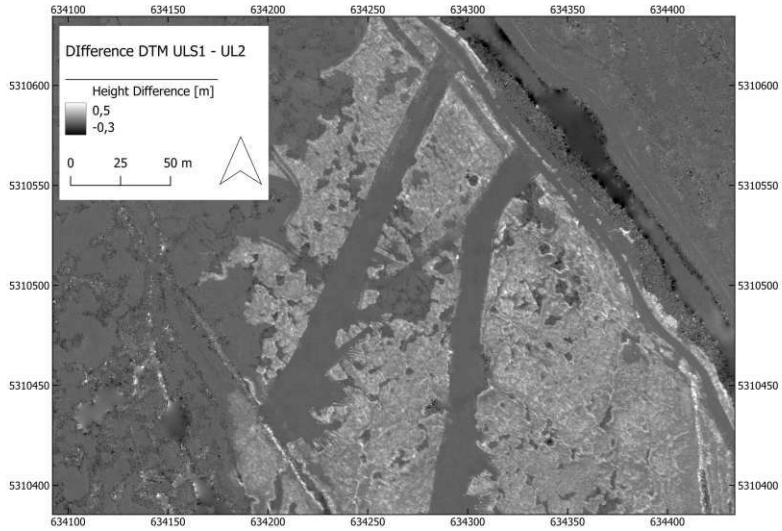


Figure 4.8: Difference DTM computed from ULS1 and ULS2 DTM, clearly showing the reduction in terrain height due to positive values in the map

Due to the low number of points on the ground during ULS3 due to dense vegetation in summer, no DTM was computed for this flight. Instead, for further analysis in ULS3, the DTM computed from ULS2 was used.

## 4.3 DSM Based Fire Area Detection

Previously indicated in Section 3.3.2, computation of the total fire area was performed after analysis of the difference between the two DSMs calculated beforehand.
A comparison between the areas outlined exposed to fire, as depicted in Figure 3.7, and the actual segmented burned areas, shown in Figure 3.6, reveals a difference of approximately 15%. The computed areas, detailed in Tab. 4.3, indicate that about 15% of the total fire-affected area did not experience complete burning. The water areas detected as described in Section 3.3.4 were also used and subtracted from the total area affected by burning ( 11%).

Table 4.3: Burning Area Statistics

| **Total Area Affected by Burning [ha]** | **Total Area Burned [ha]** | **Area Not Burned [ha]** |
|---|---|---|
| 14.68 | 12.46 | 2.22 |

## 4.4 Derived Reed Parameters

### 4.4.1 Broken Reed Layer Thickness

Regarding the In-Situ data in Section 3.2.2, 6 In-Situ sample plots have been found to be within areas that were classified as burned (12, 13, 14, 15, 17, 20). Variations in ground height within the DTM of ULS1 and ULS2 have been described previously in Section 4.2. These differences were compared with the thickness of the broken reed layer from the respective In-Situ data point.
For each of these points, the median change in DTM heights between ULS1 and ULS2 of a certain radius was taken into account and compared in Tab. 4.4. If the exact location was identified as described in Section 3.3.3 a radius of 1 m was chosen, if not a radius of 7.5 m was chosen to account for positional uncertainty. The choice of a radius of 7.5 m was made with assumptions regarding the accuracy of the handheld GNSS device compared previously in Section 3.3.3, making sure that the actual measurement site falls within the area analyzed.

Table 4.4: Thickness of In-Situ and Difference DTM Averaged Broken Reed Layer

| PNR | Thickness In-Situ [m] | Thickness DTM Median[m] |
|---|---|---|
| 12 | 0.12 | 0.14 |
| 13 | 0.19 | 0.16 |
| 14 | 0.16 | 0.14 |
| 15 | 0.19 | 0.17 |
| 17 | 0.19 | 0.16 |
| 20 | 0.19 | 0.14 |

Looking at Table 4.4, one can see that the DTM heights change between ULS1 and ULS2 in the area of the In-Situ data points. This is expected due to the reduction of the broken reed layer after the fire. Figure 4.9 also depicts that the observed change in DTM heights, to a certain extent matches the observed thickness in In-Situ measured broken reed layer thickness.

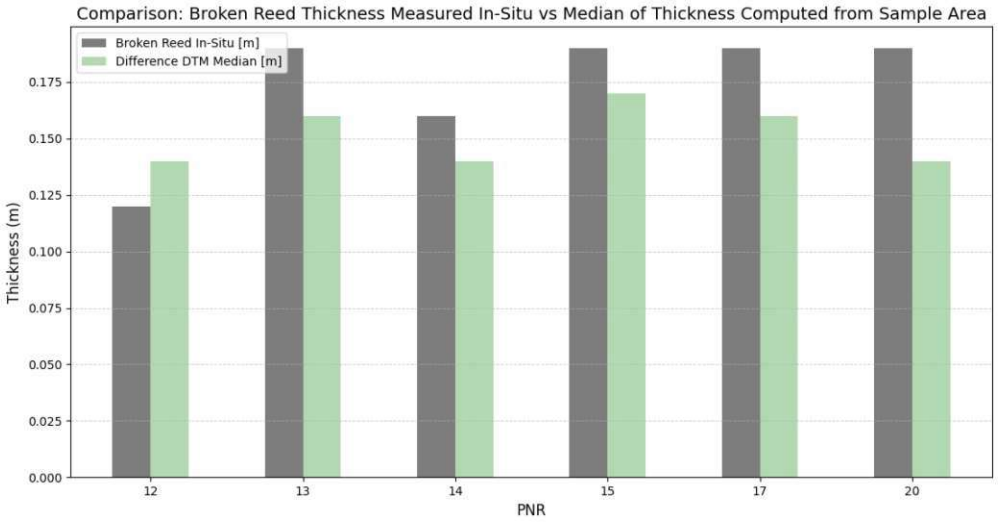


Figure 4.9: Comparison between the measured in-situ thickness of the broken reed layer and the median difference in Digital Terrain Models (DTM) from ULS1 and ULS2. The DTM difference is calculated within a 7.5 m radius around each in-situ data point if the exact location has not been identified. Where the exact location has been identified the radius was lowered to 1m.

Figures 4.15 to 4.20 show the areas where In-Situ data was collected before and after the fire. Comparing these images with Table 4.4 and Figure 4.9, changes as obvious as in the DTM height are not clearly identifiable in Figures 4.15 to 4.20.
In Figure 4.15, Figure 4.19 and Figure 4.20 as described in section 3.3.3 the data point was linked to an exact location within the UAV point cloud.
To further investigate the interaction between the broken reed layer, the ground layer and the assumed water level of 159.28 m (see Figure 3.10), a more detailed comparison between the ULS1 and ULS2 point clouds for these In-Situ data points 12, 15, 17 and 20 was performed.

Table 4.5: Comparison of Broken Reed Layer Thickness Between In-Situ Data and Point Cloud Quantile Measurement Approach

| Point Number | In-Situ Broken Reed Layer [m] | Point Cloud Broken Reed Layer [m] |
|---|---|---|
| 12 | 0.12 | 0.15 |
| 15 | 0.17 | 0.15 |
| 17 | 0.19 | 0.17 |
| 20 | 0.19 | 0.18 |

Tab. 4.5 shows, comparable results between the broken reed layer thickness observed on-site and the thickness measured within the point cloud. These values differ from those depicted

in 4.4, as they are based on the difference between the computed DTM of ULS1 and ULS2 and are not measured within the PC.
Tab. 4.6 compares the results of the ground layer thickness measured in-situ with the ground layer thickness measured from the point cloud as described in section 3.3.5. One can note that the thickness of the ground layer measured In-Situ, has a negative influence on the computed layer thickness from the point cloud. Penetration depth of the UAV LiDAR system does not seem to reach deeper than 10-15 cm within the hole. Also, when applying the previously discussed estimated water level of 159.28 m, the ground layer remains more shallow than what was measured In-Situ.

Table 4.6: Comparison of Ground Layer Thickness Between In-Situ Data and Point Cloud Measurements from ULS 2 Broken Reed Layer to Estimated Water Level of 159.28 m

| **Point Number** | **In-Situ Ground Layer [m]** | **PC Ground Layer 1% Quantile/159.28 [m]** |
|---|---|---|
| 12 | 0.25 | 0.15/0.21 |
| 15 | 0.14 | 0.15/0.19 |
| 17 | 0.30 | 0.10/0.14 |
| 20 | 0.25 | 0.10/0.14 |

Figures 4.10 to 4.13 show the point cloud in Z/X view around the location of the in-situ data collection hole. In 4.11, 4.12 as well as 4.13 one can clearly see the decrease in overall height between ULS1 (blue) and ULS2 (red). We can also observe, that for 4.11, in-situ PNr15 the 70% percentile of ULS2 (green, dotted line) is situated more at the top of the hole, due to the higher point density at the surface of ULS2. Figure 4.10, due to the presence of points on reed stems or flowers, still shows changes of the broken reed layer thickness of around 15 cm (as shown in table 4.5 and table 4.4). This shows the effective use of quantiles for specifying the limits of the hole parameters as described in 3.3.5.

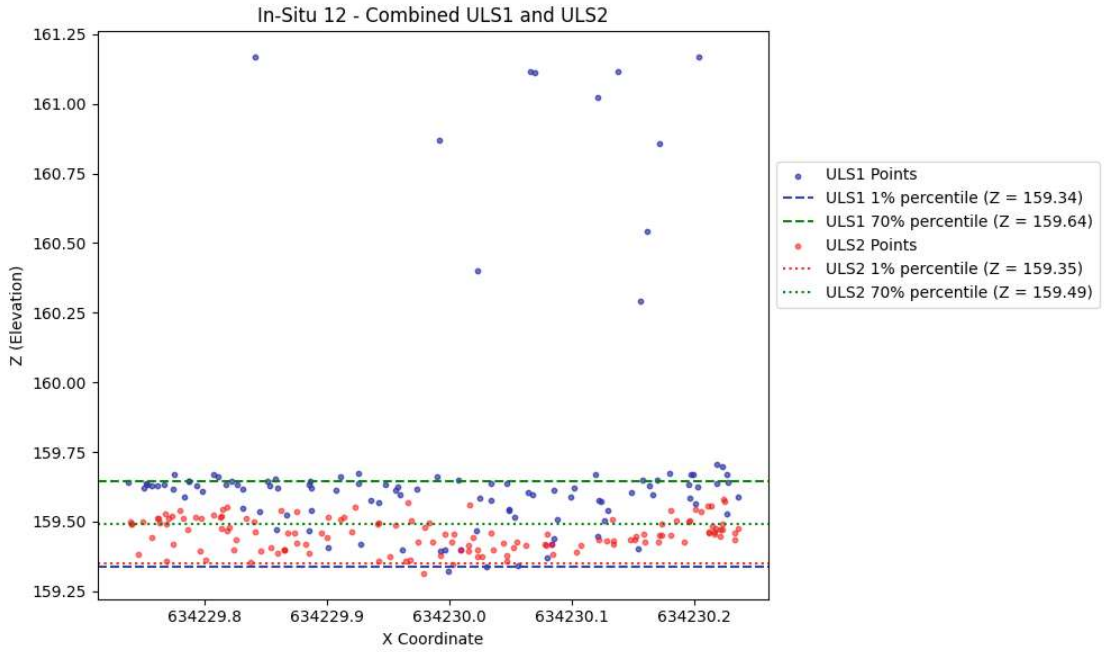


Figure 4.10: Comparison of In-Situ Point 12 Point Cloud Before and After the Fire Experiment

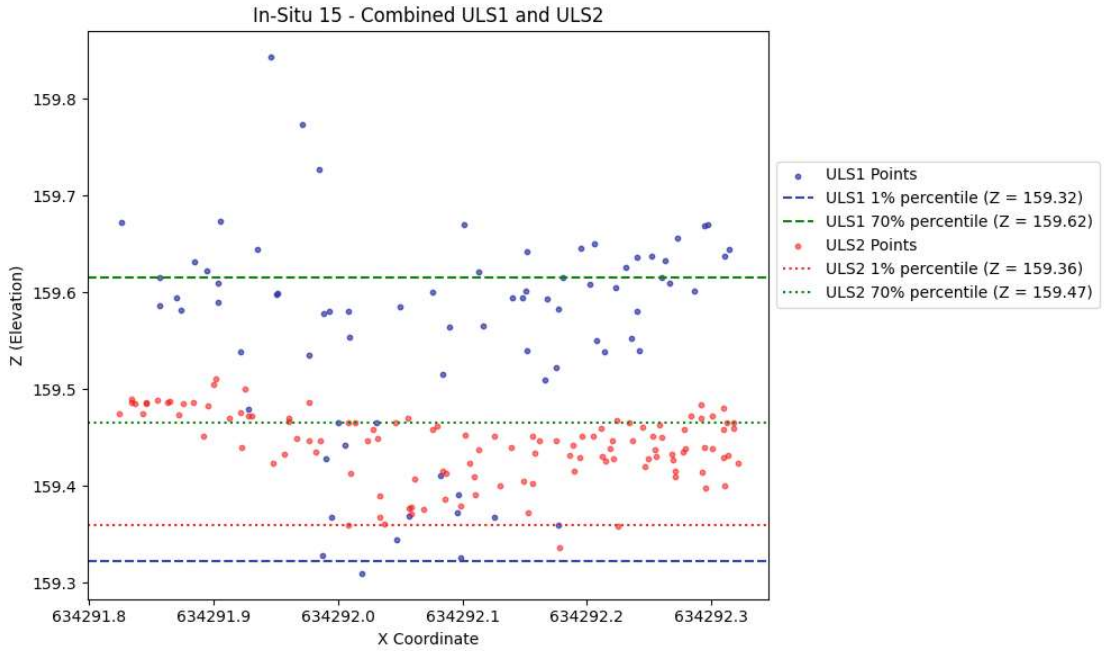


Figure 4.11: Comparison of In-Situ Point 15 Point Cloud Before and After the Fire Experiment

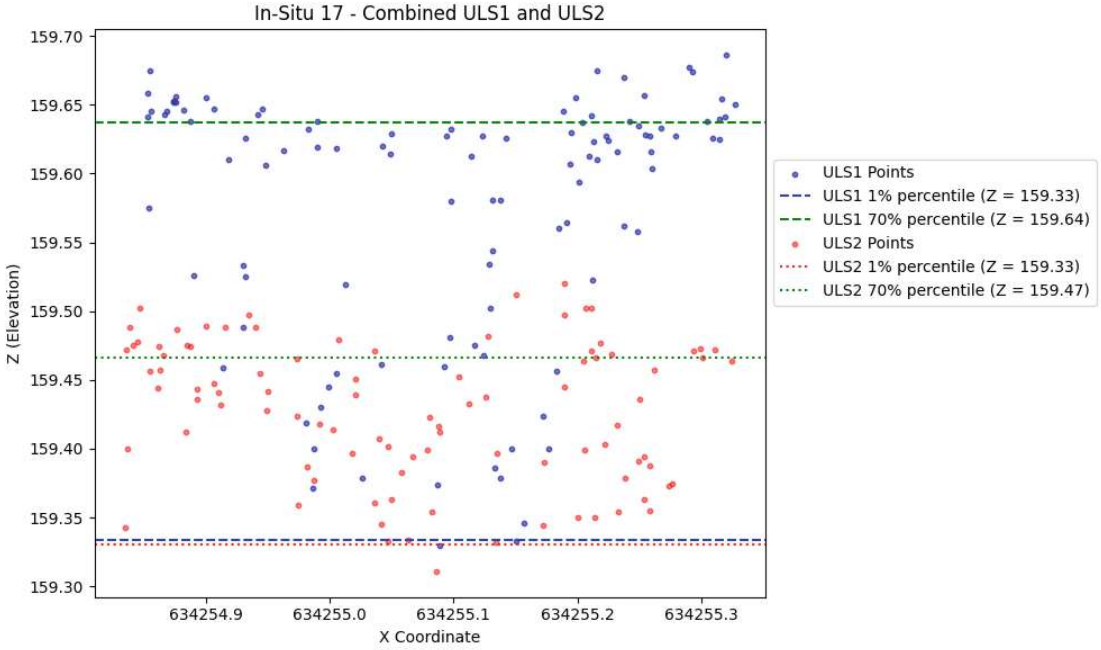


Figure 4.12: Comparison of In-Situ Point 17 Point Cloud Before and After the Fire Experiment

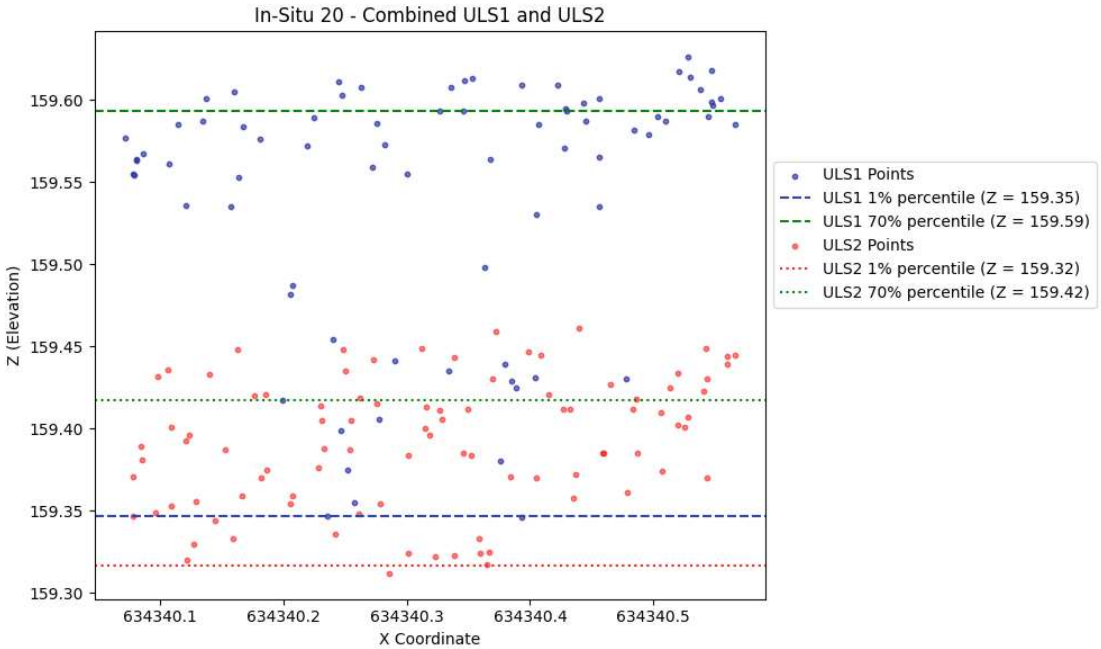


Figure 4.13: Comparison of In-Situ Point 20 Point Cloud Before and After the Fire Experiment

Figure 4.14 illustrates the comparison between the results computed from point cloud measurements and the corresponding In-Situ field measurements of both the broken reed layer and ground layer thickness. The values derived from the point cloud were computed using the scheme explained in Section 3.3.5. For the estimation of the broken reed Layer, a good fit is observed, indicating that the point cloud measurements closely align with the field data. For the Ground Layer, a clear underestimation occurs when the 1% percentile of the point cloud data is used as the representative value, as well as with an estimated water level of 159.28 m. This highlights that the ground layer thickness must be significantly deeper than the last points collected within the In-Situ measurement holes to ensure accurate estimates. The ground water itself must therefore be below 159.28 m.

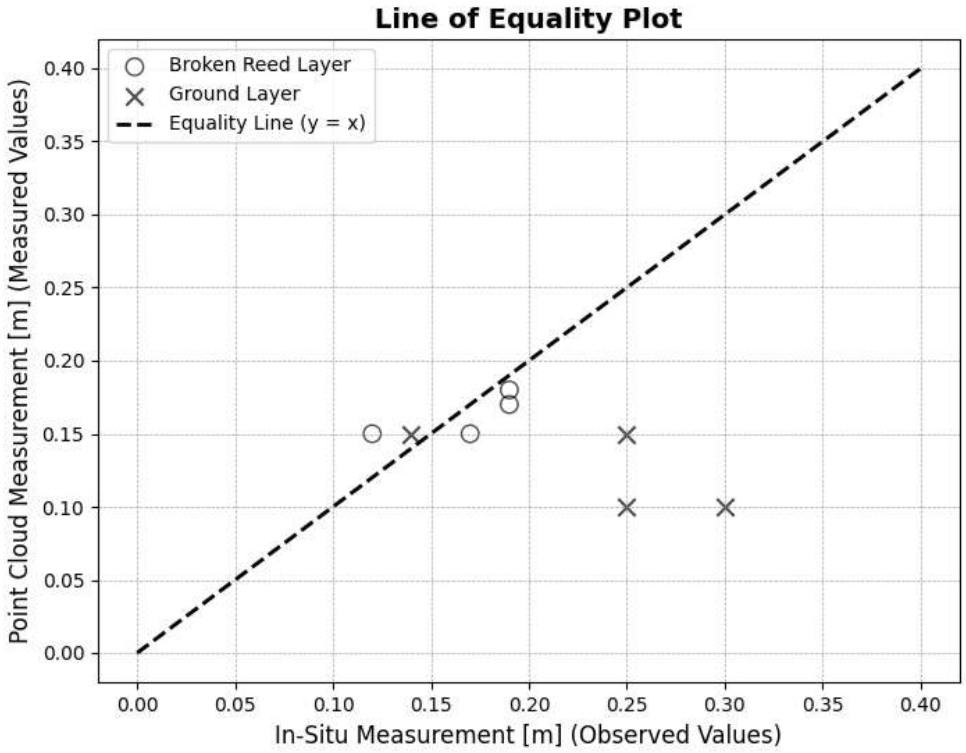


Figure 4.14: Line of equality plot showing how In-Situ Field Measurements of the Broken Reed and Ground Layer Match with the Values Obtained via Direct Measurements from the Point Cloud Using the 1%/70% Percentiles.

Two key statistical metrics were used to quantify the accuracy of the computed layer thickness values: Bias and Root Mean Square Error (RMSE), as shown in Tab. 3.8.
Here, $\Delta h_i$ represents the difference between the computed thickness (e.g., from the point cloud or difference DTM) and the corresponding In-Situ measurement for the $i$-th point, while $n$ stands for the number of samples.
The table below (Tab. 4.7) compares how different methods for estimating the broken reed

layer thickness align with the actual In-Situ measurements. The results show that using a smaller diameter to compute the median from the DTM values results in a smaller RMSE and lower bias, suggesting better agreement with the In-Situ data. Specifically, the point cloud measurement yields the lowest bias (0.00 m) and RMSE (0.03 m), followed by the 1 m Difference DTM which is close to the 7.5 m difference DTM values. It is important to note that the sample size is low as it only contains In-Situ data points where fire was present. Furthermore, sample size differs between methods, ranging from 4 samples (point cloud measurement and 1 m radius difference DTM) to 7 samples (7.5 m radius in difference DTM).

Table 4.7: This table presents the RMSE and Bias metrics resulting from the comparison between the In-Situ field measurements of the Broken Reed Layer thickness and values computed using three different methods. The 7.5 m and 1 m Difference DTM values were derived by selecting the median of all ULS1 - ULS2 DTM differences within their respective diameters, based on the localization accuracy of each In-Situ data point. The Point Cloud measurement was calculated by directly measuring the thickness in the point cloud at a resolution of 0.25x0.25 m.

| **Source** | **Bias [m]** | **RMSE [m]** |
|---|---|---|
| 7.5 m Radius Difference DTM | -0.04 | 0.05 |
| 1 m Radius Difference DTM | -0.02 | 0.04 |
| Point Cloud Measurement | 0.00 | 0.03 |

In comparison to the broken reed layer results, Tab. 4.8 shows problems in estimating the ground layer thickness. The results indicate a consistent underestimation, regardless of whether the 1% percentile or the estimated water level of 159.28 m is used for calculation. These findings can be illustrated by the trend observed in Figure 4.14, where a noticeable offset to the ground water level as measured in-situ was clearly visible.

Table 4.8: This table presents the RMSE and Bias metrics resulting from the comparison between the In-Situ field measurements of the Ground Layer thickness and values computed using two different methods. The 1% Percentile values were calculated from the point cloud directly, and the Estimated Water Level values were derived from the general estimation for the water level at the study area.

| **Source** | **Bias [m]** | **RMSE [m]** |
|---|---|---|
| 1% Percentile (Ground Layer) | -0.11 | 0.13 |
| Estimated Water Level 159.28 (Ground Layer) | -0.07 | 0.10 |

As described previously, Figure 4.15 to Figure 4.20 show the photo documentation before and after the fire, when the soil samples were collected. For all these Figures, we can see clear indications of a reduction in the broken reed layer as suggested by LiDAR data, however a mat like structure is remaining which must be attributed to the beginning of the ground

layer.

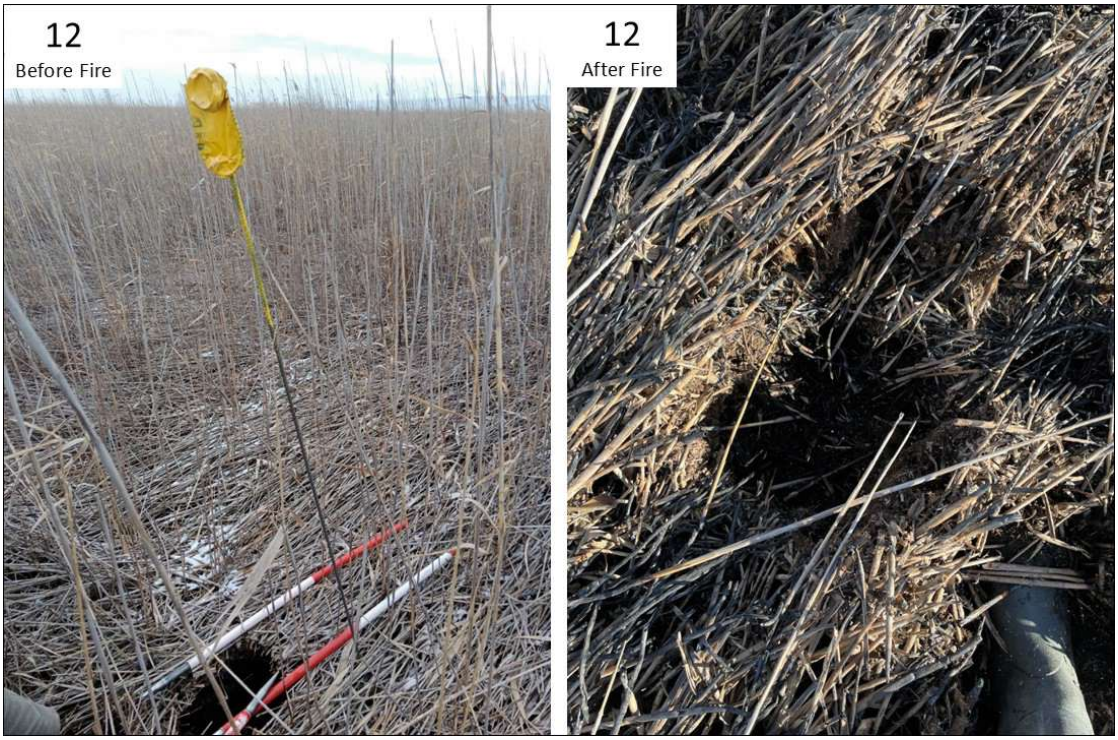


Figure 4.15: Comparison of In-Situ Point 12 Photo Documentation before and after the Fire Experiment

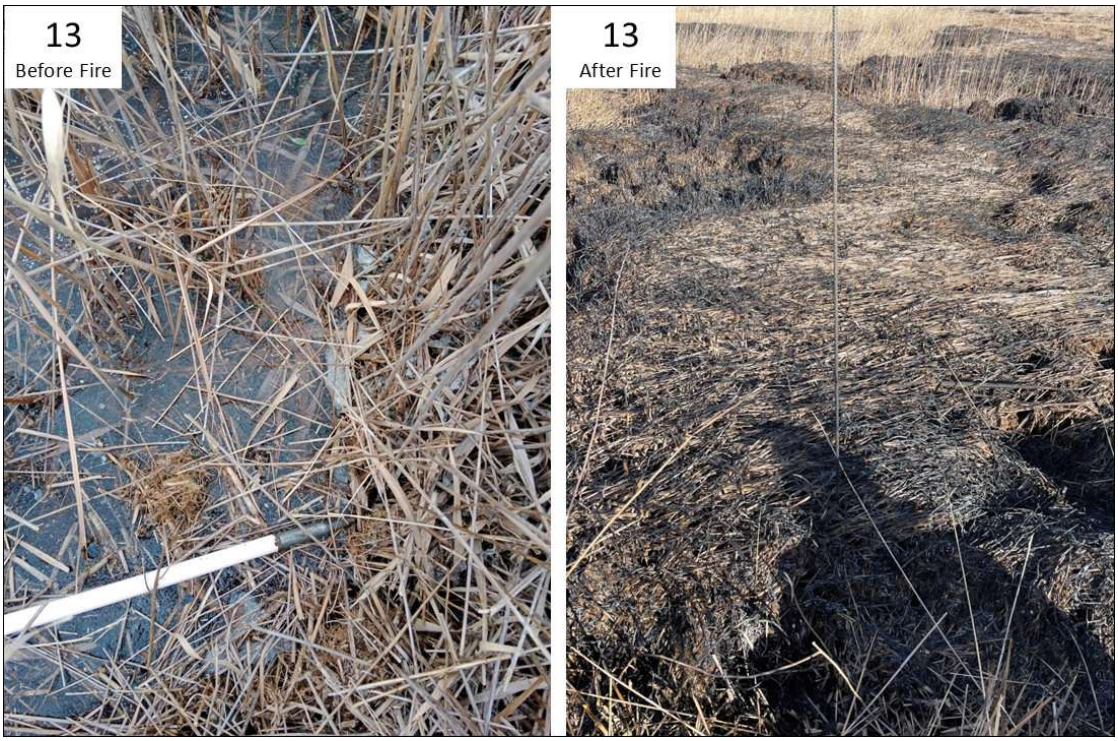


Figure 4.16: Comparison of In-Situ Point 13 Photo Documentation before and after the Fire Experiment


Figure 4.17: Comparison of In-Situ Point 14 Photo Documentation before and after the Fire Experiment

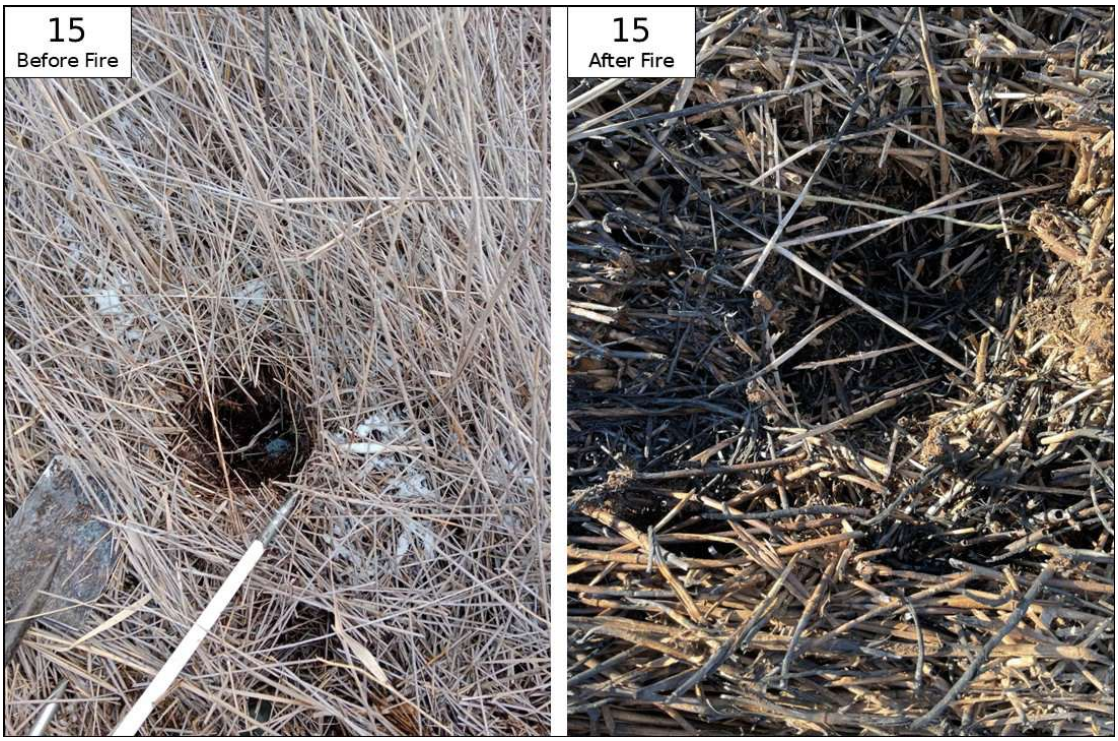


Figure 4.18: Comparison of In-Situ Point 15 Photo Documentation before and after the Fire Experiment


Figure 4.19: Comparison of In-Situ Point 12 Photo Documentation before and after the Fire Experiment

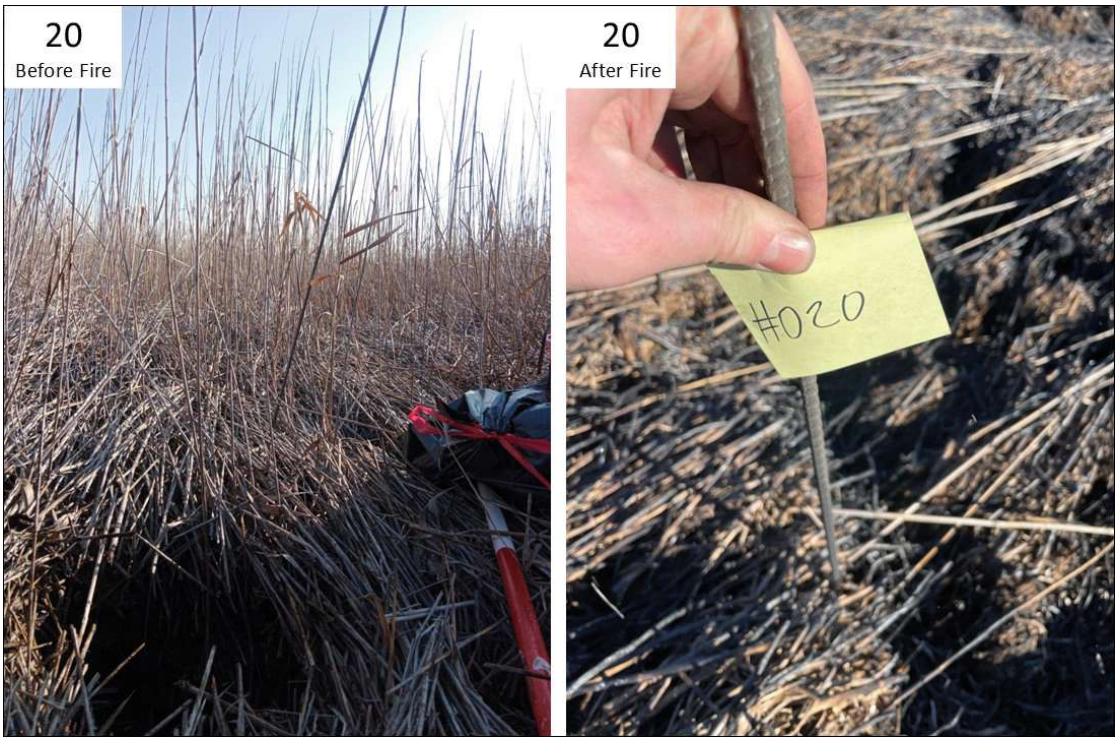


Figure 4.20: Comparison of In-Situ Point 20 Photo Documentation before and after the Fire Experiment

### 4.4.2 Reed Density

The thresholds set prior in Section 3.3.5 were used to classify the study area w.r.t. the normalized point density.

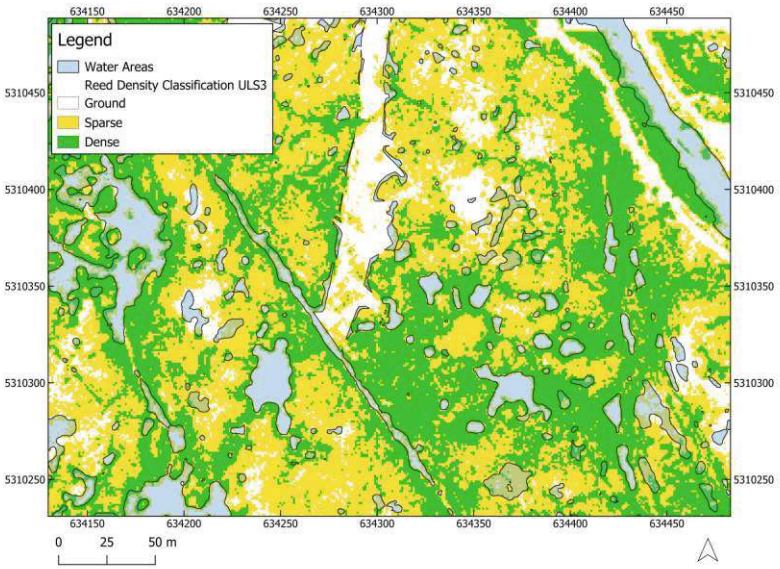


Figure 4.21: Part of the Study Area Classified into Sparse and Dense Reed with an additional Layer showing formerly Classfied Water Areas

Figure 4.21 shows a small part of the study area. The area shown has been affected by fire and there are also water areas present. We can see that areas around water are mostly surrounded by dense reed patches.

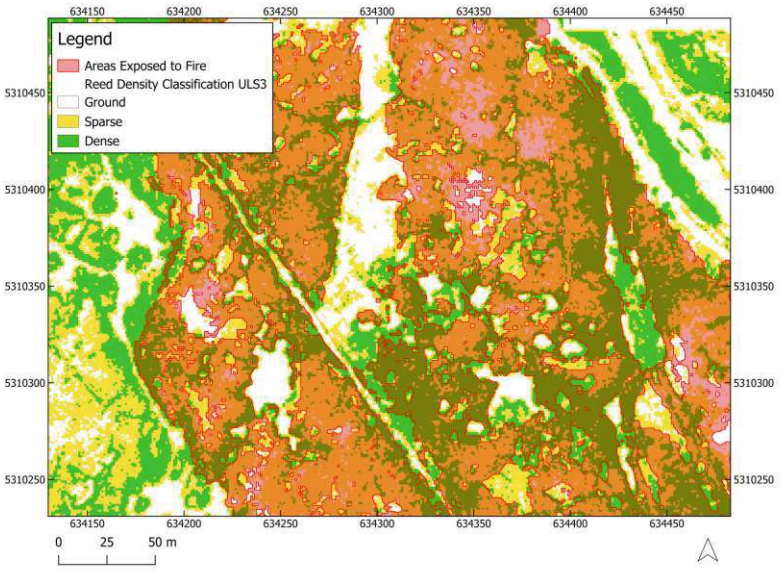


Figure 4.22: Part of the Study Area Classified into Sparse and Dense Reed with an Additional Layer Showing how Fire Affected the Area

Visualization of fire areas in the same part of the study area in Figure 4.22 shows that even in areas affected by fire, dense reed has regrown to some extent. It can also be observed that in areas not affected by fire, we can observe large areas of sparse reed.
Figure 4.23, shows the entire study area classified into sparse and dense reed patches. The main fire area remains dominated by sparse reed patches.

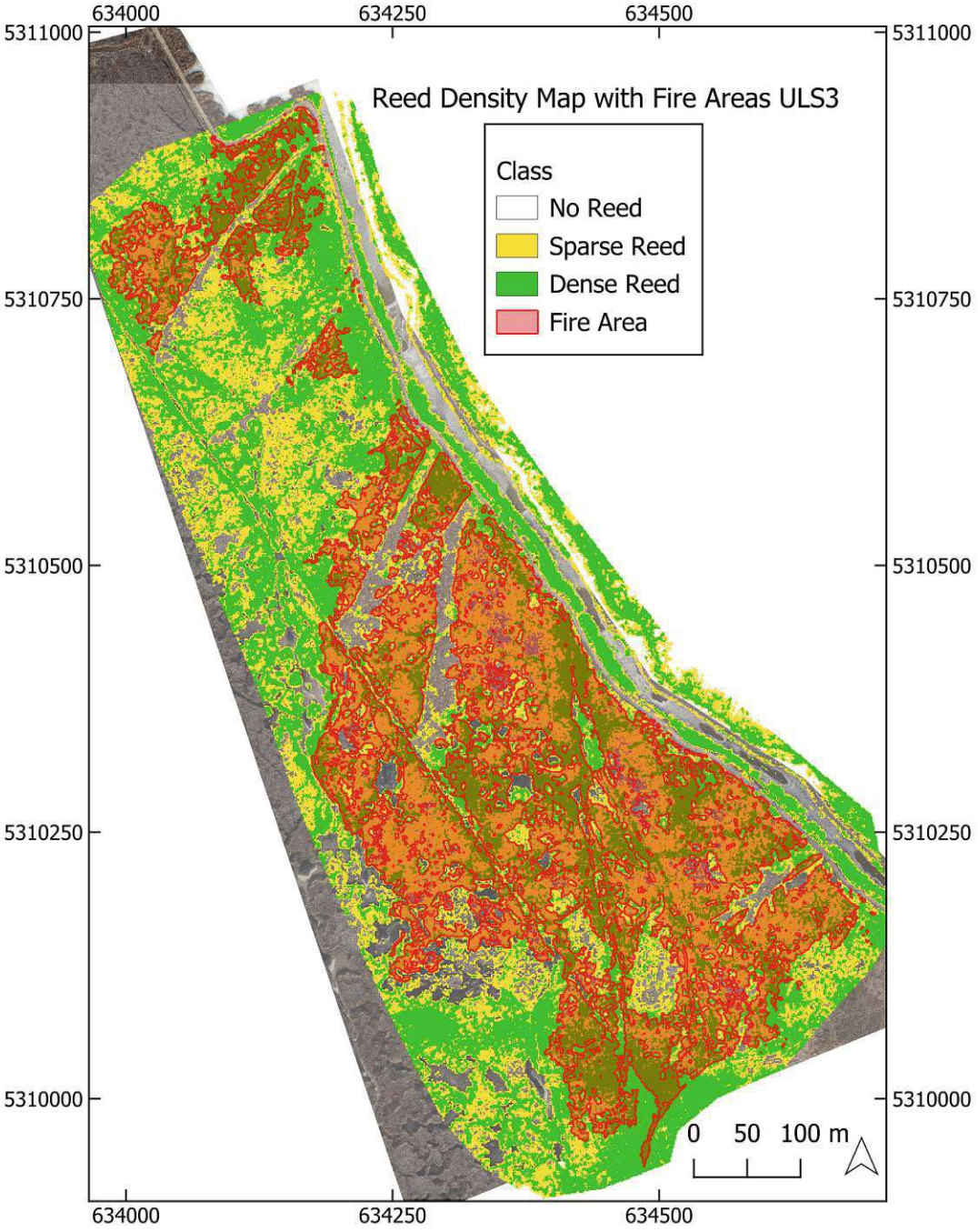


Figure 4.23: Study Area Classified into Sparse and Dense Reed with an Additional Layer Showing how Fire Affected the Area

# 5 Discussion

This study derived topographic models from ULS data in two different seasons. In addition, it provided an accurate estimate for the derived DSMs, which was subsequently used to compute estimations for fire-affected areas as well as water areas. After computing the difference DTMs, a quantification of the broken reed layer was successfully performed using In-Situ data for validation of the results. Point density estimations were used to identify sparse and dense reed stands throughout the study area.
In the discussion that follows, the key findings are examined in detail, exploring their methodological strengths and limitations as well as their potential for future research.

## 5.1 In Situ Data

In Situ Data was collected at various locations as described in Section 3.2.2. The use of low-accuracy GNSS handheld devices made an accurate and meaningful incorporation difficult for most In-Situ data points. As described in the methodology in Section 3.2.2, the process of retrieving the exact In-Situ locations from the point cloud was challenging. Only 8 out of 20 sample locations were successfully linked to their location within the point cloud. More samples with links to their exact location could have strengthened the analysis with respect to the broken reed layer.
In addition, also the computation of reed heights could have benefited from more precise coordinates (RTK quality). More precise coordinates for In-Situ data points would have meant more references for assessing the vertical accuracy. Future work should therefore prioritize the use of RTK GNSS or other high-precision devices to ensure precise geolocation of In-Situ points
The In-Situ points were spread over the whole study area. This meant not all of them were affected by fire leading to the broken reed layer validation with less than 50% of the reference data. Concentrating some In-Situ data points in an area with high probability of burning could have led to a more thorough analysis regarding the layer thickness reduction.

## 5.2 Derived Reed Parameters

### 5.2.1 Reed Heights at In-Situ Locations measured on DSM

The DSM provides valuable information, particularly when normalized with an accurate DTM. However, as observed in Section 4.1.1, DSM height values do not always precisely represent reed heights. Although flat surfaces generally yield an accurate representation of the surface, the situation is different in areas with reed stands. Increasing the grid size, as demonstrated in Tab. 4.2, significantly improves vertical accuracy for reed stands. However, we can observe reduced accuracy for flat objects, as shown in Tab. 4.1. Therefore, the choice

of DSM grid size must be chosen according to the specific objectives of the analysis. In terms of reed height estimation, especially in winter months, a larger grid size is recommended. As discussed previously, the sparse point cloud representing the reed crown, due to the absence of leaves, results in an irregular vertical representation of reed stalks. Using a larger grid size reduces these effects by weakening the influence of individual reed stalks on the overall representation.
Another factor that generally reduces the accuracy of reed height representation is the dynamic nature of reed structures. Movement caused by wind can lead to stalks being captured multiple times, at different locations across different flight paths, affecting the consistency of the generated DSM (Corti Meneses et al., 2017).
For the summer campaign ULS3, no accuracy metrics were computed due to the absence of In-Situ reference points for height comparison. However, in terms of the accuracy of flat structures, the results are expected to align with those presented in Tab.4.1. As discussed in Tab. 4.4.2, the denser vegetation during the summer months results in a point cloud with a concentration of points at the canopy level and very few ground points. This denser and more uniform vegetation distribution likely allows the use of a smaller grid size when generating a DSM for summer conditions, as the more uniform canopy could reduce the variability previously observed in the winter measurement campaign.

### 5.2.2 Removal of Reed Mats

The removal of reed mats is a key goal in reintroducing fire management for reed management purposes (Nemeth et al., 2022).
The results on the reduced thickness of the broken reed layer and the ground layer indicate that fire management effectively reduces the thickness of the broken reed layer when burning occurs. As shown in Section 4.2, a reduction in DTM height is clearly visible after visualizing the difference DTM (Figure 4.8). This confirms that fire management reduces the broken reed layer. However, we lack definitive proof that the layer is completely removed during the process due to insufficient data on the exact thickness of the layer across the study area. As described in Section 3.2.2, the thickness of this layer can vary significantly, reaching up to 1m. Thus, the difference DTM alone cannot conclusively confirm the complete elimination of the layer.
Nevertheless, the results presented in Section 4.4.1 further support the argument that the broken reed layer may have been reduced significantly. Discrepancies between the thickness observed at the in-situ data points and the corresponding values derived from the point cloud are expected due to various contributing factors.
These factors include inaccuracies within the point cloud measurement methodology used for evaluating results (illustrated in Section 4.4.1), errors in the In-Situ measurements, and inaccuracies in the DTM itself. A particular challenge lies in identifying the starting point of the measurements. The quantiles chosen for evaluation may not accurately reflect the

true starting point of the layer, and thus the computed differences may not fully capture the extent of the layer.
While fine-resolution point cloud measurements taken at the hole where In-Situ data was collected allow for comparisons with the field data, a raster-based approach is more efficient for large-scale studies, as the grid size of 1 m or more allows for more efficient computation. For In-Situ measurements, deviations caused by the use of a ruler to assess the broken reed layer (i.e., the burnable layer) are possible. In addition, the transition between the broken reed layer and the ground layer is expected to overlap to some extent.
For large-scale analyses, the difference DTM could be an effective tool to determine where the broken reed layer was reduced or eliminated. However, an accurate DTM is essential as the foundation for correct analysis. As previously discussed in Section 3.3.1, computing the DTM required specific parameter tuning to represent the bottom layer accurately, when vegetation vegetation cover was denser. Determining the exact ground level remains challenging due to the uneven surface of the broken reed and the resulting difficulties in defining the "ground". In the pre-fire DTM, the terrain reference likely aligns with the top of the broken reed layer, as to a certain extent this layer is not penetrable. The post-fire DTM, assuming complete reduction of the broken reed layer, should reference the ground.
Therefore, the difference DTM can be seen as an effective tool for evaluating and measuring the reduction of the broken reed layer over large areas after a fire event, but its complete elimination can only be confirmed with sufficient field measurements. The density of the reed in the vegetative season means that to collect data for DTM generation, data collection must take place in the winter months with little leaf cover.

### 5.2.3 Reed Density

Using ULS data acquired in summer, our study classified reed patches into dense and sparse patches based on relative point density thresholds. Normalizing the point density, successfully removed flight patterns within the ULS data. It was found that dense patches tend to be located around water areas, while sparse reeds were identified where affected by fire. However, dense patches have also regrown in areas previously affected by fire as well as sparse patches situated in areas not affected by fire.
We would expect to see more clear distinction between areas affected by fire and areas that have not been affected. Other studies achieved good results classifying dense and sparse patches using point density and rank statistics in their workflows, using a very strategic placement of validation profiles In-Situ, in order to test the classifier (Corti Meneses et al., 2017). In our study, In-Situ data points, providing information on the number of reed stalks could not be used for analysis, as no correlation between point density and the number of reed stalks was found. In order to further evaluate this method and improve the parameters, validation data is essential to assess accuracy.
Given further improvements and validation, the point density could be a valuable metric on

how the reed habitat is developing after fire management. To provide further information on the status before the fire, a ULS flight in the vegetative season prior to such an experiment is recommended. Pre-fire ULS data in winter, due to little vegetation, cannot be used for sparse or dense classification. In addition, reed belts classified as sparse or dense could provide further indication of potential areas suited for fire management. The analysis of reed density, if applied in a time series over a larger period of time could be used to monitor changes in reed structure.

## 5.3 DSM Based Fire Area Detection

The analysis of fire areas using difference DSMs from before and after the fire revealed that of all areas affected by fire (enclosed), 15% did not fully burn (Tab. 4.3). In a large fire event in marshlands in Poland with an area of 5500 hectares it was estimated that 90% of the surface vegetation (consisting of dead reed to a large part) was removed because of the fire (Walesiak et al., 2022). This suggests our results to be a realistic estimate, given the size difference of the fires.

The Estimation was based on difference DSMs and a threshold for the height reduction. This threshold was set to 80 cm. In return, this would mean that burned objects below the size of the threshold are not detectable by this method, potentially missing areas that have experienced burning with lower vegetation. In contrast, a high threshold also assures detection when reed is burned.

Aerial image collection after the fire, in conjunction with the ULS2 data collection could have provided validation data to assess the quality of the fire area estimation. Validation could also be performed by setting up "validation" profiles that need to be investigated before and after the fire. However, this would mean a substantial amount of field work.

Quantifying the extent of unburned areas within fire-affected regions is important to evaluate the efficiency of fire management strategies and provides a planning basis for future projects. The results suggest that even in a controlled burning environment, effects will differ throughout fire management areas, and complete burning should not be expected.

# 6 Conclusion

The presented work has demonstrated that UAV LiDAR can be used to quantify how the broken reed layer can be affected by fire management. Topographic models such as DTM and DSM were computed and used to visualize changes in broken reed layer thickness as well as mapping areas affected by burning in between two ULS campaigns in January 2024 (ULS1 and ULS2).

Height changes observed in DTMs can be used to depict changes in broken reed layer thickness throughout a large study area. In-Situ data points were used for validation and a RMSE of below <5 cm could be achieved.

A third measuring campaign (ULS3) was performed in August 2024 in order to further monitor the development of the reed belt after the fire event. ULS3 was used to classify reed stocks in the study area based on their normalized point density into sparse and dense reed. However, the absence of in-situ reference data for validation limits the certainty of these classifications. Further monitoring of the area w.r.t. the reed density is recommended, in order to monitor how the reed belt is recovering from fire management and if further positive effects such as increased density throughout the study area can be observed.

# A Source Code

## A.1 Code use in Software OPALS

### Topographic Models (DSM, DTM, nDSM)

```

:: DSM Computation - Generates a Digital Surface Model from the ULS point cloud
opalsDSM -inf ULS_pointcloud.odm -outf ULS_pointcloud_DSM100.tif -grids 1

:: General Workflow for DTM Generation:
:: 1. Thinning step: Extracts the lowest last echo points within a small raster cell
:: 2. Hierarchical iterative approach: Processes from coarse to fine resolution
opalscell -inf ULS_pointcloud.odm -outf ULS_pointcloud_min005.odm -cellsize 0.05 -feat min -filter echo[last]

:: Generate a coarse DTM with a quantile filter (removes outliers)
opalscell -inf ULS_pointcloud_min005.odm -outf ULS_pointcloud_min3.odm -cellsize 3 -feat quantile:0.05

:: Interpolate using Delaunay Triangulation
opalsgrid -inf ULS_pointcloud_min3.odm -outf ULS_pointcloud_min3_tr.tif -interpol delaunayTriangulation -grids 1 -searchra 5

:: Fill gaps using triangulation
opalsfillgaps -inf ULS_pointcloud_min3_tr.tif -outFile ULS_pointcloud_min3_tr_fg.tif -method triangulation

:: Add normalized height information to points
opalsaddinfo -inf ULS_pointcloud_min005.odm -gridf ULS_pointcloud_min3_tr_fg.tif -attribute "normalizedZ=z-r[0]" -points_in_memory 999000000 -nbthreads 1
```

Listing 1: Computation of Topographic Models (DSM, DTM, nDSM)

### Watermask Computation

```
:: Create Water Mask - Extract areas based on a specified height range
opalsAlgebra -infile ULS_pointcloud_DTM_final_sr05_neigh10_fg_adaptive.tif -outfile ULS_pointcloud_watermask_dtm_09_015.tif -formula "r[0] >= 159.3 - .3 && r[0] <= 159.3 + 0.15 ? 1 : 0"
```

```
3
4  :: Smooth watermask using a majority filter
5  opalsStatfilter -inf ULS_pointcloud_watermask_dtm_09_015.tif -
       outFile ULS_pointcloud_watermask_dtm_09_015_majority10.tif -
       feature majority -kernelSize 10 -kernelShape diamond
6
7  :: Binarize the watermask for further processing
8  opalsAlgebra -inFile ULS_pointcloud_watermask_dtm_09_015_majority10.
       tif -outFile
       ULS_pointcloud_watermask_dtm_09_015_majority10_binary.tif -
       formula "r[0] >= 1.5 ? 1 : 0"
9
10 :: Create shapefile for the watermask area
11 opalsContouring -infile
       ULS_pointcloud_watermask_dtm_09_015_majority10_binary.tif -
       outfile ULS_pointcloud_watermask_dtm_09_015_majority10.shp
```

Listing 2: Watermask Computation

### Fire Area Classification

```
1  :: Compute DSM Difference for Fire Area Detection
2  opalsAlgebra -inf ULS1_pointcloud_DSM100.tif ULS2_pointcloud_DSM100.
       tif -outf ULS_pointcloud_DSM_100_diff.tif -formula "r[0]-r[1]"
3
4  :: Detect Fire Areas Based on Height Differences
5  opalsAlgebra -infile ULS_pointcloud_DSM_100_diff.tif -outfile
       fire_areas_dsm100_080.tif -formula "r[0]>.8 ? 1 : 0"
6
7  :: Smooth Fire Area Mask
8  opalsStatfilter -inf fire_areas_dsm100_080_080.tif -outFile
       fire_areas_dsm100_080_maj1.tif -feature majority -kernelSize 1 -
       kernelShape diamond
9
10 :: Binarize and Extract Fire Area Shapes
11 opalsAlgebra -inFile fire_areas_dsm100_080_maj1.tif -outFile
       fire_areas_dsm100_080_maj1_bin.tif -formula "r[0] >= 1.5 ? 1 : 0"
12
13 :: Extract Fire Area Shapefiles by Minimum Area
14 opalsContouring -infile fire_areas_dsm100_080_maj1_bin.tif -outfile
       fire_areas_dsm100_080_maj1_bin_minarea_1.shp -minarea 1
15 opalsContouring -infile fire_areas_dsm100_080_maj1_bin.tif -outfile
       fire_areas_dsm100_080_maj1_bin_minarea_100.shp -minarea 100
```

Listing 3: Fire Area Classification

### In-Situ Data Export

```
:: Export Data for Plotting and In-Situ Analysis
opalsView -inFile ULS_pointcloud_insitu5.odm -filter "region
    [634141.98 5310698.759 634145.021 5310700.259]"

:: Export Small, Medium, and Large Plots for Analysis
opalsExport -inFile ULS_pointcloud.odm -filter "generic[X >=
    634143.480 - 0.25 AND X <= 634143.480 + 0.25 AND Y >= 5310699.509
     - 0.25 AND Y <= 5310699.509 + 0.25]" -outFile
    ULS_pointcloud_insitu5_00625m2.odm

opalsExport -inFile ULS_pointcloud.odm -filter "generic[X >=
    634143.480 - 0.5 AND X <= 634143.480 + 0.5 AND Y >= 5310699.509 -
     0.5 AND Y <= 5310699.509 + 0.5]" -outFile
    ULS_pointcloud_insitu5_1m2.odm

:: Export for Plotting in Other Software
opalsexport -inf ULS_pointcloud_insitu5_00625m2.odm -outf
    ULS_pointcloud_insitu4_00625m2.xyz
```

Listing 4: In-Situ Data Export

### Point Density Normalization

```
:: Calculate First Echo Point Density
opalsCell -inFile ULS_pointcloud.odm -outFile
    ULS_pointcloud_first_echoes_pdens.tif -feature pdens -cellSize 1
    -filter Echo[First] -points_in_memory 999000000 -nbthreads 1

:: Calculate Above-Ground Point Density (NormalizedZ > 1m)
opalsCell -inFile ULS_pointcloud.odm -outFile
    ULS_pointcloud_first_echoes_above_100cm_pdens.tif -feature pdens
    -cellSize 1 -filter "Echo[First] AND Generic[NormalizedZ > 1]" -
    points_in_memory 999000000 -nbthreads 1

:: Normalize Point Density by Above-Ground Points
opalsAlgebra -inFile ULS_pointcloud_first_echoes_pdens.tif
    ULS_pointcloud_first_echoes_above_100cm_pdens.tif -outFile
    ULS_pointcloud_normalized_density_100cm.tif -formula "r[1]/r[0]"
```

Listing 5: Point Density Normalization

### A.1.1 Python

#### Quantile Based Broken Reed Layer Thickness Estimation

```
1
2
3  def insitu_hole_parameters_diff(directory_uls1, directory_uls2,
       save_dir):
4      # Define the directory where results will be saved
5      save_dir = save_dir
6      os.makedirs(save_dir, exist_ok=True)  # Create the directory if
       it doesn't exist
7
8      # Helper function to extract in-situ number from filename
9      def get_insitu_number(filename):
10         match = re.search(r'insitu(\d+)', filename)
11         return match.group(1) if match else None
12
13     # Get all .xyz files from both directories
14     files_uls1 = {get_insitu_number(f): os.path.join(directory_uls1,
       f)
15                   for f in os.listdir(directory_uls1) if f.endswith(
       '.xyz')}
16     files_uls2 = {get_insitu_number(f): os.path.join(directory_uls2,
       f)
17                   for f in os.listdir(directory_uls2) if f.endswith(
       '.xyz')}
18
19     # Find matching pairs of files by in-situ number
20     common_insitu_numbers = set(files_uls1.keys()).intersection(
       files_uls2.keys())
21
22     # Create or open the result text file
23     result_file_path = os.path.join(save_dir, "
       percentile_differences.txt")
24     with open(result_file_path, "w") as result_file:
25         # Write the header line
26         result_file.write("In-Situ Number\tULS1 1%\tULS2 1%\tULS1
       70%\tULS2 70%\tDifference 70%\tDifference 70%-1%\n")
27
28         for insitu_number in common_insitu_numbers:
29             # Load the data for matching in-situ number
30             file_path_uls1 = files_uls1[insitu_number]
31             file_path_uls2 = files_uls2[insitu_number]
32
33             df_uls1 = pd.read_csv(file_path_uls1, delim_whitespace=
       True, names=["X", "Y", "Z"])
34             df_uls2 = pd.read_csv(file_path_uls2, delim_whitespace=
```

```
    True, names=["X", "Y", "Z"])
35
36              # Calculate 1% and 70% percentiles for ULS1 and ULS2
37              percentiles = [0.01, 0.70]
38              uls1_percentile_values = {p: df_uls1['Z'].quantile(p)
    for p in percentiles}
39              uls2_percentile_values = {p: df_uls2['Z'].quantile(p)
    for p in percentiles}
40
41              # Calculate the difference between the 70% percentiles
42              difference_70_percentile = uls1_percentile_values[0.70]
    - uls2_percentile_values[0.70]
43
44              # Calculate the difference between the 70% percentile
    and the lower of the 1% percentiles for ULS1 and ULS2
45              lower_1_percentile = min(uls1_percentile_values[0.01],
    uls2_percentile_values[0.01])
46              difference_70_1_percentile = uls1_percentile_values
    [0.70] - lower_1_percentile
47
48              # Write the results to the text file
49              result_file.write(f"In-Situ {insitu_number}\t"
50                                f"{uls1_percentile_values[0.01]:.2f}\t
    {uls2_percentile_values[0.01]:.2f}\t"
51                                f"{uls1_percentile_values[0.70]:.2f}\t
    {uls2_percentile_values[0.70]:.2f}\t"
52                                f"{difference_70_percentile:.2f}\t{
    difference_70_1_percentile:.2f}\n")
53
54     print(f"Differences have been calculated and saved to {
    result_file_path}")
55
56 # Example usage
57 # insitu_hole_parameters_diff("path/to/ULS1_directory", "path/to/
    ULS2_directory")
```

Listing 6: Script for Quantile Based Estimation of Broken Reed Thickness

# B Use of Generative AI

AI-based tools like ChatGPT and Writefull were used in the development of this thesis for purposes including coding and grammar checking. In general, the guidelines on the responsible use of general artificial intelligence in research and their recommendations to researchers were closely followed (European Commission Directorate-General for Research and Innovation, Directorate E-Prosperity, Unit E4 - Industry 5.0 & AI in Science, 2024).

# References

Antoniazza, M., Clerc, C., Le Nédic, C., Sattler, T., & Lavanchy, G. (2018). Long-term effects of rotational wetland mowing on breeding birds: Evidence from a 30-year experiment. *Biodiversity and Conservation*, *27*(3), 749–763. https://doi.org/10.1007/s10531-017-1462-1

Baier, S., Corti Meneses, N., Geist, J., & Schneider, T. (2022). Assessment of Aquatic Reed Stands from Airborne Photogrammetric 3K Data. *Remote Sensing*, *14*(2), 337. https://doi.org/10.3390/rs14020337

BEV - Bundesamt für Eich- und Vermessungswesen. (2024). *Höhengrid bev*. https://www.bev.gv.at/Services/Produkte/Grundlagenvermessung/Hoehen-Grid.html

Corti Meneses, N., Baier, S., Geist, J., & Schneider, T. (2017). Evaluation of Green-LiDAR Data for Mapping Extent, Density and Height of Aquatic Reed Beds at Lake Chiemsee, Bavaria—Germany. *Remote Sensing*, *9*(12), 1308. https://doi.org/10.3390/rs9121308

Corti Meneses, N., Brunner, F., Baier, S., Geist, J., & Schneider, T. (2018). Quantification of Extent, Density, and Status of Aquatic Reed Beds Using Point Clouds Derived from UAV–RGB Imagery. *Remote Sensing*, *10*(12), 1869. https://doi.org/10.3390/rs10121869

Csaplovics, E., & Schmidt, J. (2009). *Schilfkartierung neusiedler see: Ausdehnung und struktur der schilfbestände des neusiedler sees – projektmanagement, erfassung und kartierung des österreichischen anteiles durch luftbildklassifikation* (tech. rep.) (Abschlussbericht. Auftraggeber: Österreichischer Naturschutzbund – Landesgruppe Burgenland. Auftragnehmer: Technische Universität Dresden. Bearbeiter: Prof. Dr. habil. Elmar Csaplovics, Dipl.-Ing. Jana Schmidt). Technische Universität Dresden, Fakultät Forst-, Geo- und Hydrowissenschaften, Professur für Geofernerkundung.

Dinka, M., Ágoston-Szabó, E., & Szeglet, P. (2010). Comparison between biomass and C, N, P, S contents of vigorous and die-back reed stands of Lake Fertő/Neusiedler See. *Biologia*, *65*(2), 237–247. https://doi.org/10.2478/s11756-010-0006-x

Doughty, C. L., & Cavanaugh, K. C. (2019). Mapping Coastal Wetland Biomass from High Resolution Unmanned Aerial Vehicle (UAV) Imagery. *Remote Sensing*, *11*(5), 540. https://doi.org/10.3390/rs11050540

Dronova, I., Kislik, C., Dinh, Z., & Kelly, M. (2021). A Review of Unoccupied Aerial Vehicle Use in Wetland Applications: Emerging Opportunities in Approach, Technology, and Data. *Drones*, *5*(2), 45. https://doi.org/10.3390/drones5020045

Dvorak, M., Bieringer, G., Braun, B., Grüll, A., Karner-Ranner, E., Kohler, B., Korner, I., Laber, J., Nemeth, E., Rauer, G., & Wendelin, B. (2016). Bestand, Verbreitung und Bestandsentwicklung gefährdeter und ökologisch bedeutender Vogel- arten im Nationalpark Neusiedler See - Seewinkel: Ergebnisse aus den Jahren 2001 bis 2015.

European Commission Directorate-General for Research and Innovation, Directorate E-Prosperity, Unit E4 - Industry 5.0 & AI in Science. (2024, March). Living guidelines on the responsible use of generative ai in research [First edition. The European Commission shall not be liable for any consequence stemming from the reuse.].

Gallant, A. (2015). The Challenges of Remote Monitoring of Wetlands. *Remote Sensing*, *7*(8), 10938–10950. https://doi.org/10.3390/rs70810938

Grosser, S., Pohl, W., & Melzer, A. (1997). *Untersuchung des schilfrückgangs an bayerischen seen: Forschungsprojekt des bayerischen staatsministeriums für landesentwicklung und umweltfragen* (Vol. 141). Bayerisches Landesamt für Umweltschutz.

Hackl, P., & Ledolter, J. (2023). A Statistical Analysis of the Water Levels at Lake Neusiedl. *Austrian Journal of Statistics*, *52*(1), 87–100. https://doi.org/10.17713/ajs.v52i1.1444

Höhle, J., & Höhle, M. (2009). Accuracy assessment of digital elevation models by means of robust statistical methods. *ISPRS Journal of Photogrammetry and Remote Sensing*, *64*(4), 398–406. https://doi.org/10.1016/j.isprsjprs.2009.02.003

Hollaus, M., Mandlburger, G., Pfeifer, N., & Mücke, W. (2010). Land cover dependent derivation of digital surface models from airborne laser scanning data. *IAPRS*, *XXXVIII, Part 3A*, 27–29.

Huete, A., Didan, K., Miura, T., Rodriguez, E., Gao, X., & Ferreira, L. (2002). Overview of the radiometric and biophysical performance of the MODIS vegetation indices. *Remote Sensing of Environment*, *83*(1-2), 195–213. https://doi.org/10.1016/S0034-4257(02)00096-2

Hydrographischer Dienst Burgenland. (2024a). *Precipitation station neusiedl january 2024*. https://wasser.bgld.gv.at/hydrographie/der-niederschlag/neusiedl-am-see

Hydrographischer Dienst Burgenland. (2024b). *Water level station breitenbrunn january 2024*. https://wasser.bgld.gv.at/hydrographie/die-seen/breitenbrunn

Lin, Y.-C., Cheng, Y.-T., Zhou, T., Ravi, R., Hasheminasab, S., Flatt, J., Troy, C., & Habib, A. (2019). Evaluation of UAV LiDAR for Mapping Coastal Environments. *Remote Sensing*, *11*(24), 2893. https://doi.org/10.3390/rs11242893

Luo, S., Wang, C., Xi, X., Pan, F., Qian, M., Peng, D., Nie, S., Qin, H., & Lin, Y. (2017). Retrieving aboveground biomass of wetland Phragmites australis (common reed) using a combination of airborne discrete-return LiDAR and hyperspectral data. *International Journal of Applied Earth Observation and Geoinformation*, *58*, 107–117. https://doi.org/10.1016/j.jag.2017.01.016

Nemeth, E., & Dvorak, M. (2022). Reed die-back and conservation of small reed birds at Lake Neusiedl, Austria. *Journal of Ornithology*, *163*(3), 683–693. https://doi.org/10.1007/s10336-022-01961-w

Nemeth, E., Dvorak, M., Glaser, F., Kohler, B., & Schwienbacher, M. (2022). *Entwicklung nachhaltiger schilferntetechniken und monitoring schilfgürtel neusiedler see* (Projek-

tendbericht). Amt der Burgenländischen Landesregierung Abt. 4, Hauptreferat Naturschutz und Landschaftspflege.

Nemeth, E., & Grubbauer, P. (2005). Zur aktuellen Bestandssituation der Reiher und Löffler des Neusiedler See-Gebietes. (48), 1–18.

Neumann. (2024). In-situ data parameters collected by students of university of vienna [Unpublished data].

Onojeghuo, A. O., & Blackburn, G. A. (2011). Optimising the use of hyperspectral and LiDAR data for mapping reedbed habitats. *Remote Sensing of Environment*, *115*(8), 2025–2034. https://doi.org/10.1016/j.rse.2011.04.004

Schaefer, M., & Pearson, A. (2021). Accuracy and precision of GNSS in the field. In *GPS and GNSS Technology in Geosciences* (pp. 393–414). Elsevier. https://doi.org/10.1016/B978-0-12-818617-6.00002-0

Song, P., Zheng, X., Li, Y., Zhang, K., Huang, J., Li, H., Zhang, H., Liu, L., Wei, C., Mansaray, L. R., Wang, D., & Wang, X. (2020). Estimating reed loss caused by Locusta migratoria manilensis using UAV-based hyperspectral data. *Science of The Total Environment*, *719*, 137519. https://doi.org/10.1016/j.scitotenv.2020.137519

Van Der Putten, W. H. (1997). Die-back of Phragmites australis in European wetlands: An overview of the European Research Programme on Reed Die-back and Progression (1993–1994). *Aquatic Botany*, *59*(3-4), 263–275. https://doi.org/10.1016/S0304-3770(97)00060-0

Walesiak, M., Mikusiński, G., Borowski, Z., & Żmihorski, M. (2022). Large fire initially reduces bird diversity in Poland's largest wetland biodiversity hotspot. *Biodiversity and Conservation*, *31*(3), 1037–1056. https://doi.org/10.1007/s10531-022-02376-y

Zlinszky, A., Mücke, W., Lehner, H., Briese, C., & Pfeifer, N. (2012). Categorizing Wetland Vegetation by Airborne Laser Scanning on Lake Balaton and Kis-Balaton, Hungary. *Remote Sensing*, *4*(6), 1617–1650. https://doi.org/10.3390/rs4061617